ARCHIVES
MASSACHUSETTS INSTITUTE OF TECHNOLOGY
JUN 17 2015
LIBRARIES

Novel Terahertz and Nanophotonic Lasers: theory, design, and fabrication

by

Jeongwon Lee

B.Eng. Materials Science and Engineering, Pohang University of Science and Technology, Korea, 2009

Submitted to the Department of Materials Science and Engineering in partial fulfillment of the requirements for the degree of

DOCTOR OF PHILOSOPHY

at the

MASSACHUSETTS INSTITUTE OF TECHNOLOGY

February 2015

© Massachusetts Institute of Technology 2015. All rights reserved.

Signature redacted

Author .....
Department of Materials Science and Engineering
November 25th, 2014

Signature redacted

Certified by .....
Marin Soljačić
Professor of Physics and MacArthur Fellow
Thesis Supervisor

Signature redacted

Accepted by .....
Donald Sadoway
Chair, Departmental Committee on Graduate Students

MIT Libraries

77 Massachusetts Avenue
Cambridge, MA 02139
http://libraries.mit.edu/ask

DISCLAIMER NOTICE

Due to the condition of the original material, there are unavoidable flaws in this reproduction. We have made every effort possible to provide you with the best copy available.

Thank you.

The images contained in this document are of the best quality available.

Novel Terahertz and Nanophotonic Lasers: theory, design, and fabrication

by

Jeongwon Lee

Submitted to the Department of Materials Science and Engineering
on November 25th, 2014, in partial fulfillment of the
requirements for the degree of
DOCTOR OF PHILOSOPHY

Abstract

In this thesis, we will explore numerical modeling and fabrication of laser sources.

First, we demonstrate and distinguish experimentally the existence of special type of Fano resonances at $k \approx 0$ in a macroscopic two-dimensional photonic crystal slab. We fabricate a square lattice array of holes in silicon nitride layer and perform an angular resolved spectral analysis of the various Fano resonances. We elucidate their radiation behavior using temporal coupled-mode theory and symmetry considerations. The unique simplicity of this system whereby an ultra-long lifetime delocalized electromagnetic field can exist above the surface and consequently easily interact with added matter, provides exciting new opportunities for the study of light and matter interaction. However, we confirmed that achievable quality factor (Q) is limited by fabrication imperfection. Therefore, in the second part, we present an extensive fabrication optimization process, through which we established improved Q by a factor of three.

Lastly, we report a comprehensive theoretical analysis and new experimental data of high-pressure (> 1 Torr) lasing action in optically-pumped far-infrared (OPFIR) lasers. No previous models could satisfactorily capture high-pressure operation because of the growing role of excited vibrational levels. Without these additional excited vibrational levels, molecules are artificially trapped in lower energy vibrational levels. This, in turn, prematurely triggers the so-called vibrational bottleneck and quenches the lasing action at low pressures in the previous models. Even though the high-pressure behavior can be more realistically modeled by including numerous excited vibrational levels, it would dramatically increase the computation time, and more importantly, the rate constants connecting all these levels are unknown. We propose a new model with an expandable pool which embodies 120 excited vibrational levels. Moreover, the knowledge of state-to-state rates among the excited vibrational levels is unnecessary in the proposed new model since the net rate related to the expandable level can be found by equilibrium conditions. Together with a detailed calculation of the pump rate and the wall collision rate, our model qualitatively and quantitatively reproduces experimentally measured high-pressure behavior. The

model can be universally used for any OPFIR gas laser system. Thus, our work puts forward a theoretical formalism that could enable the advancement of compact terahertz radiation sources.

Thesis Supervisor: Marin Soljačić
Title: Professor of Physics and MacArthur Fellow

Acknowledgments

First and foremost I would like to thank my advisor Professor Marin Soljačić, for his continual guidance, inspiration, and support over the years. In the time I have had the privilege to work with Marin, his mentorship has instilled in me a sense of what it means to do great science and be a inspiring leader, and he will always remain a role model for me.

I would also like to thank the members of my thesis committee, Professor Jannopoulos, Professor Fink, and Professor Fitzgerald, for their time and dedication to this thesis. I also thank Professor Henry Everitt for years of collaboration on THz laser modeling project.

Thanks to the members of the Marin's group; I am honored to have had the opportunity to work with such a brilliant group of researchers, and people. Special thanks goes to Bo Zhen, Ognjen Ilic, Chia Wei Hsu, Adrian Y.X.Yeng, Song Liang Chua, Wenjun Qiu, and Yichen Shen - for their sincere friendship and fruitful discussions.

I especially thank Yongjoo Kim and Sungjae Ha for motivating me from the very beginning to come to MIT, and being the biggest supporters of my graduate years. I also thank Changmin Lee, Jouha Min, Sooyeon Huh, Hyangsoo Jeong, Hokyung Choi, Jooyeon Kim, Donghun Kim, Grace Han, Sungjune Kim, Hongchul Jang, Chungjong Yu, Jungmin Lee, Junwon Choi, Jaejin Kim, Jeongyun Kim, and Gyuweon Hwang for their great freindship. I wish to express my warm thanks to all members in HSSH-MIT, POSTECH-MIT, and KGMSE for sharing and supporting enjoyable graduate life at MIT.

Finally, I am forever grateful to my family. Thanks to my parents Joong Jae Lee and Soon Joo Kang and my brother Jeonghun Lee for their constant love and support. I would also like to thank Kwang Chool Lee, Younghee Kim, and Jeein Lee. Finally though, I owe most gratitude to Juei Lee for inspiring me to be a better person, and for sticking by me no matter what through every moment of struggling and every step of achievement. This thesis would have not been possible without their unconditional and unparalleled love.

Contents

List of Figures

Chapter 1

Overview

Technology advancements in the past decades have enabled the design and fabrication of structures at length scales comparable to, or even smaller than the wavelength of light. The interaction of light with these nanoscale features such as photonic crystal cavities leads to the tight confinement of light and significantly enhanced light-matter interactions. Recent advances in computational power and high capacity data storage have also enabled the numerical simulation of complicated light-matter interactive systems. This provides numerous opportunities to build a theoretical model and understand the physical mechanisms of the considered system. In this thesis, we will explore novel fabrication and numerical simulation techniques to build and deeply understand the light-matter interaction in laser systems.

In chapter 2, we demonstrate and distinguish experimentally the existence of special type of Fano resonances in PhCs with quality factors that could, in principle, approach infinity despite lying within the light cone [1]. These *non-degenerate* Fano resonances are delocalized modes that decouple from the light cone states at $\mathbf{k}$=0 due to symmetry considerations. A clear distinction between these modes and *degenerate* Fano resonances with finite Q^{total} at the Γ point is presented by fabricating a square lattice array of holes in silicon nitride layer and performing an angular resolved spectral analysis of the various Fano resonances. From the analysis, we found that achievable Q^{total} is limited by non-radiative Q which comes from fabrication imperfection, which motivated our second study.

In chapter 3, we present a fabrication route for centimeter-scale two-dimensional defect-free photonic crystal slabs with quality factors bigger than 10,000 in the visible, together with a unique way to quantify their quality factors [2]. We fabricate Si_3N_4 photonic crystal slabs, and perform an angle-resolved reflection measurement. This measurement data is used to retrieve the quality factors of the slabs by fitting it to a model based on temporal coupled-mode theory. The fabrication steps that we established here improved Q by a factor of three from the previous study in chapter 2. We further confirmed that IL is a more suitable method to fabricate macroscopically large PhCs in terms of cost and time efficiency, compared to e-beam lithography. We believe the fabrication route can be further improved by expanding the IL laser beams to a wider angle or by shaping the beam profile to a more uniform distribution. Then spatial power distribution will become uniform, and spatial variation of the pattern will be decreased. Post-process thin dielectric film coating using atomic layer deposition might also improve Q.

From chapter 2 and 3, the experimental realization of this special type of Fano resonance modes has several important consequences: 1) the strongly enhanced field close to the PhC surface and the simple access to it provides a new platform for the study of light and matter interaction; 2) it offers an easy-to-fabricate structure that supports delocalized modes with ultrahigh quality factors; 3) it can be shown from coupled mode theory that up to 50% of external radiation can be coupled to these strongly confined modes in symmetric PhC slabs, when one ensures that the Q-matching condition between the radiative life-time, and the absorptive life-time is satisfied; and 4) despite the macroscopically large area resonator, only a few high-Q modes are supported within a fairly broad frequency range. The delocalized nature of this mode is particularly important in applications where the interaction of an enhanced electric field with a macroscopic volume of matter can dramatically improve the performance of the process, such as in bimolecular sensing and organic light emitting devices. Furthermore, the realization of this novel resonance could enable the enhancement and the demonstration of new physical phenomena in laser physics, energy conversion, nonlinear optics, and optical filters, as demonstrated in [3–5].

In chaper 4, we report a methodology to simulate high-pressure lasing action of optically pumped far-infrared (OPFIR) lasers. As pressure increases, the molecular population in excited vibrational levels increases because it becomes difficult to diffuse toward the wall and be de-excited to the ground state through wall collision. This so-called vibrational bottleneck decreases pump rate and quenches the lasing action, resulting in pump power insensitive cutoff pressure. This phenomenon was observed from previous models with limited number of vibrational levels, which contradicts experimental observations. Even though the vibrational bottleneck can be circumvented by including numerous excited vibrational levels, it would exponentially increase the computation time and more importantly, the rate constants connecting all these levels are unknown. We propose a new model with a single expandable level which embodies numerous vibrational levels. This is advantageous in that it requires very small number of vibrational levels, while mimicking the environment with numerous levels. Also, the knowledge of state-to-state rates among the excited vibrational levels is unnecessary since the net rate related to the expandable level can be found by equilibrium conditions. Together with more sophisticated definition of the pump rate and the wall collision rate, our model qualitatively and quantitatively reproduces experimentally measured high-pressure behavior. The model can be universally used for any OPFIR laser gas systems, and we believe that this report could contribute to the development of room-temperature atmospheric-pressure compact sources of far-infrared and terahertz radiation.

Chapter 2

Observation and differentiation of unique high-Q optical resonances near zero wavevector in macroscopic photonic crystal slabs

2.1 Introduction

The realization of high quality factor cavities in photonic crystals has led in the past two decades to experimental observations of novel physical phenomena in both fundamental and applied research [6–17]. Modes supported by such cavities fall into two categories: 1) pure modes with infinite lifetimes that lie outside the light cone and 2) resonant modes with finite lifetimes that lie within the light cone and consequently can couple to radiation modes. A proposed surprising exception to the latter involves special Fano resonances of a macroscopic two-dimensional periodic photonic crystals slab, whose lifetimes are predicted to approach infinity as their crystal wavevector, $\mathbf{k}$, approaches zero within the light cone [18–20]. The only possibility for these special Fano resonances to completely decouple from the continuum of free-space modes is by mismatching their symmetries. It is the periodic nanostructure that determines the

symmetry of the modes and the macroscopic large area that enables their approaching-to-infinity lifetime. Here, we employ a centimeters square photonic crystal slab to demonstrate and *distinguish* $\mathbf{k}\approx 0$ non-degenerate Fano resonances with quality factors as high as 10^4 that extend over 10^8 unit cells. The photonic crystal, fabricated using interference lithography, consists of a square lattice array of holes in Si_3N_4 layer with periodicity of 320 nm. Through angle-resolved spectral measurements and temporal coupled-mode theory, we determined the resonances' quality factors and the various physical mechanisms that govern their value. Using symmetry considerations, we elucidate the behavior of the different resonances at $\mathbf{k}\approx 0$. The physical origin of Fano resonances in PhC slabs lies in the coupling between the guided modes supported by the slab and external plane waves, which occurs because of the periodic modulation of the dielectric constant. Typically all these Fano resonances have long lifetimes or high quality factors (Q), but there is a special subset of them whose Q's have been proposed to approach infinity. In theory, in a perfect infinite periodic PhC slab, due to symmetry considerations, very unusual Fano 'resonances' at $\mathbf{k}=0$ have been predicted to completely decouple from the external world with infinite radiative quality factor (Q_{rad}) despite lying within the light cone [18–20]. For $\mathbf{k}$ near zero, these unique guided resonances have ultra-long (but finite) lifetime, providing an efficient means to couple light in and out of the slab. In practice due to the finite size of any experiment, the incoming and outgoing beams always include wavevectors with $\mathbf{k}>0$, and hence the resonance lifetime is finite. Although this very unique behavior of Fano resonances in PhC slabs has been discussed theoretically [18–21], experimental verification of high-Q Fano resonances near $\mathbf{k}=0$ over a macroscopically large area has yet to be demonstrated. The key challenge in observing these resonances is that in practical structures, in addition to limits imposed by material absorption, fabrication imperfections partially break the crystal symmetry which results in coupling of these Fano resonances to radiating modes. In addition, the mode itself needs to extend over a macroscopic area in order to support high Q_{rad}, posing a significant fabrication challenge.

2.2 Sample fabrication

Realizing high quality-factor resonances in photonic nano-structures requires both the careful consideration of the bulk material properties and the sub-wavelength structure geometry. Material absorption sets the upper bound of the attainable quality factor, while the structure geometry can be optimized to minimize scattering due to surface roughness and non-uniformities of the periodic structure. A favorable candidate for achieving high quality factor resonances in the visible is a slab of Si_3N_4 deposited on top of microns thick oxide layer of a silicon wafer [22]. With refractive index of 2.02, Si_3N_4 provides sufficient index contrast with the SiO_2 below and air or fluids on top. The Si_3N_4 layer was grown by low-pressure chemical vapor deposition (LPCVD) on top of 6 μm thermally grown SiO_2 layer on a silicon wafer (from Lionix). Using a prism coupler, we measured propagation losses in the Si_3N_4 layer to be less than 0.3 dB/cm at 632 nm.

We fabricated large area square lattice PhC with periodicity of 320 nm and unit cell consisting of a 55 nm deep, 160 nm in diameter cylindrical hole in a 250 nm thick Si_3N_4 layer. Fig. 2-1 shows the fabrication process. The process started by depositing a trilayer resist stack, which consists of a negative photoresist (PR) layer, an SiO_2 intermediate layer, and an antireflection coating (ARC). The thickness of the ARC layer was optimized to minimize back reflection to the PR layer during lithography. The PhC pattern was produced by the interference lithography (IL) system using a 325 nm He/Cd laser. In the IL system, the laser beam is split into two and then interfered to form a standing wave with a period of $\lambda/(2\sin\theta)$. A second exposure with the sample rotated by 90° relative to the first exposure defines the two-dimensional grid pattern on the PR layer. The period of the pattern is determined by the angle of incidence, while the diameter of the hole is determined by the exposure dose. After the exposure, the sample was developed in a commercial PR developer. Pattern transfer from the PR layer through the SiO_2 and ARC layers to the Si_3N_4 layer was achieved with reactive ion etching (RIE). CF_4 gas was used to etch the SiO_2 and the Si_3N_4 layers, and He/O_2 gas was used to etch the ARC layer. Due to the

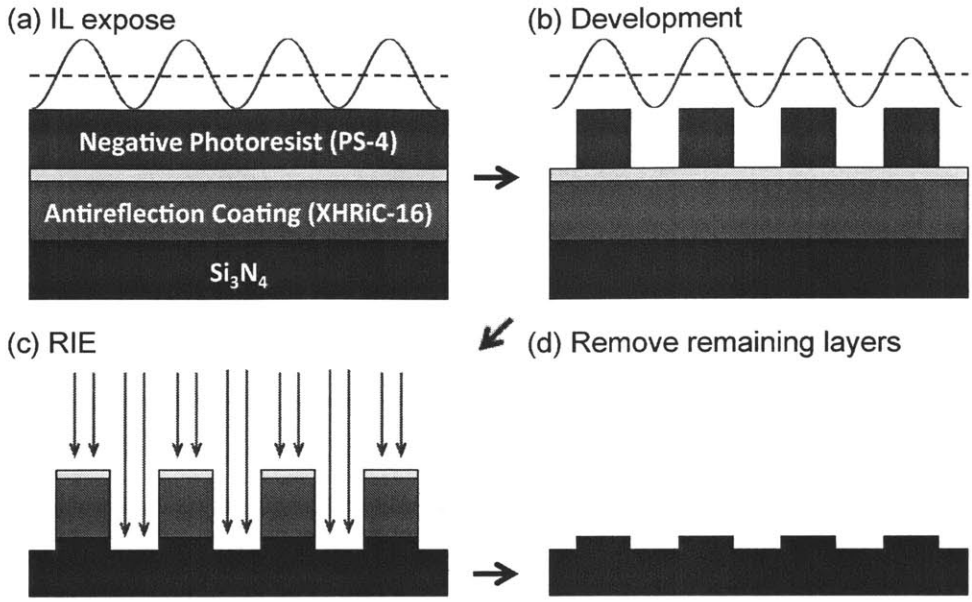

Figure 2-1: Illustration of 2D PhC fabrication process. (a) PR is exposure using IL, (b) PR development, (c) pattern transfer using RIE, and (d) removal of the remaining stack.

anisotropic characteristic of RIE, vertical and smooth sidewalls were produced as well as relatively small lateral roughness compared to wet etched samples. The average period of the pattern and the average hole diameter both had standard deviation of 6 nm. Uniform periodic patterns were obtained on samples as large as 3 cm^2. For the optical characterization however a smaller sample was needed due to size constrain of the cell used to mount the sample. Thus all measurements shown in here were obtained from 0.7×0.7 cm^2 sample. SEM images of the final sample is shown in Fig. 2-2.

2.3 Sample characterization

We performed optical characterization of the PhC slab using a super-continuum laser source (SuperK Compact, NKT Photonics) with spot size of 2 mm at small incident angles, measured from the normal to the PhC plane. (Fig. 2-3) The PhC slab was placed in a precision liquid cell containing toluene (n=1.49), representing a potential future incorporation of the slab into fluidic systems for organic lasers and sensing

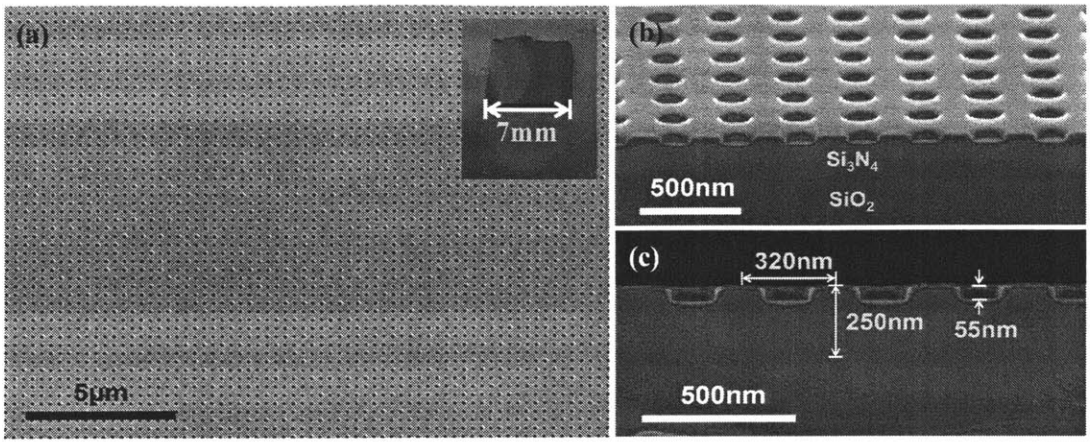

Figure 2-2: SEM images of the fabricated PhC. (a) Top-view, (b) Tilt-view, and (c) Side-view SEM images of the fabricated PhC. The structure is made of a 250 nm thick Si_3N_4 with periodic cylindrical holes on top of 6 μm thick SiO_2 layer with average period of 320 nm, average hole diameter of 160 nm, and average hole depth of 55 nm. The inset shows an image of the sample of around 7×7 mm^2. The pattern is defined all over the area.

applications. The liquid cell was mounted on a precision motorized rotating stage (ESP300, Newport) with a resolution of 0.01°. A schematic of the experimental setup is shown in the inset of Fig. 2-4(a). Passing through a beam splitter, the laser beam is back-reflected from the PhC slab at an angle set by the horizontally rotating stage and collected by a spectrometer with a resolution of 0.03 nm (HR4000, Ocean optics). The polarization of the randomly polarized incoming beam was set using a polarizer to be either E_x (horizontal) or E_y (vertical). Fig. 2-4(a) and 2(d) depict the reflection spectra measured for each of the polarizations at 61 different angles between 0° and 2° (measured from the normal towards the x-axis). The reflection spectra reveal eight energy bands.

2.4 Finite-difference time-domain simulation

To corroborate these results we used finite difference time domain simulation [23] to calculate the modes of the PhC. The computational cell consisted of a 250 nm thick Si_3N_4 with refractive index of n = 2.02 on top of an "infinitely" thick layer of SiO_2 (n = 1.45). Hole with depth of 55 nm and diameter of 160 nm was introduced in

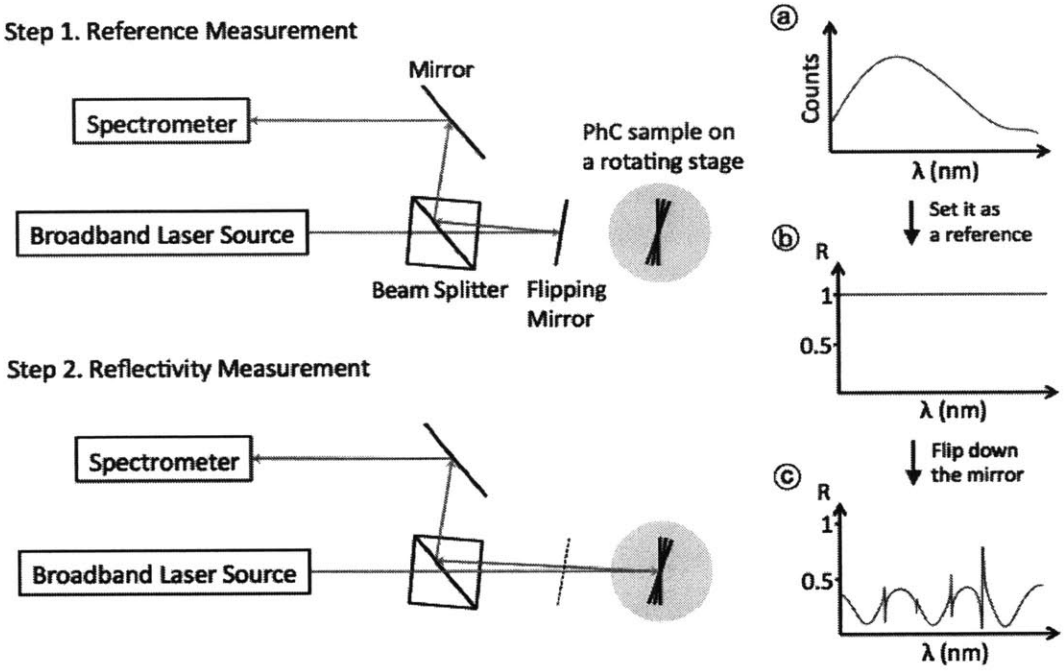

Figure 2-3: Optical measurement setup. The setup consists of a broadband laser source, a rotating stage, and a spectrometer. To obtain the reflectivity of the sample, a beam splitter and a flipping mirror was placed between the laser source and the stage. ⓐ: Spectrum of the laser source, ⓑ: measurement mode is changed to a reflectivity mode, ⓒ: spectrum of light reflected from the sample after flipping mirror is flipped.

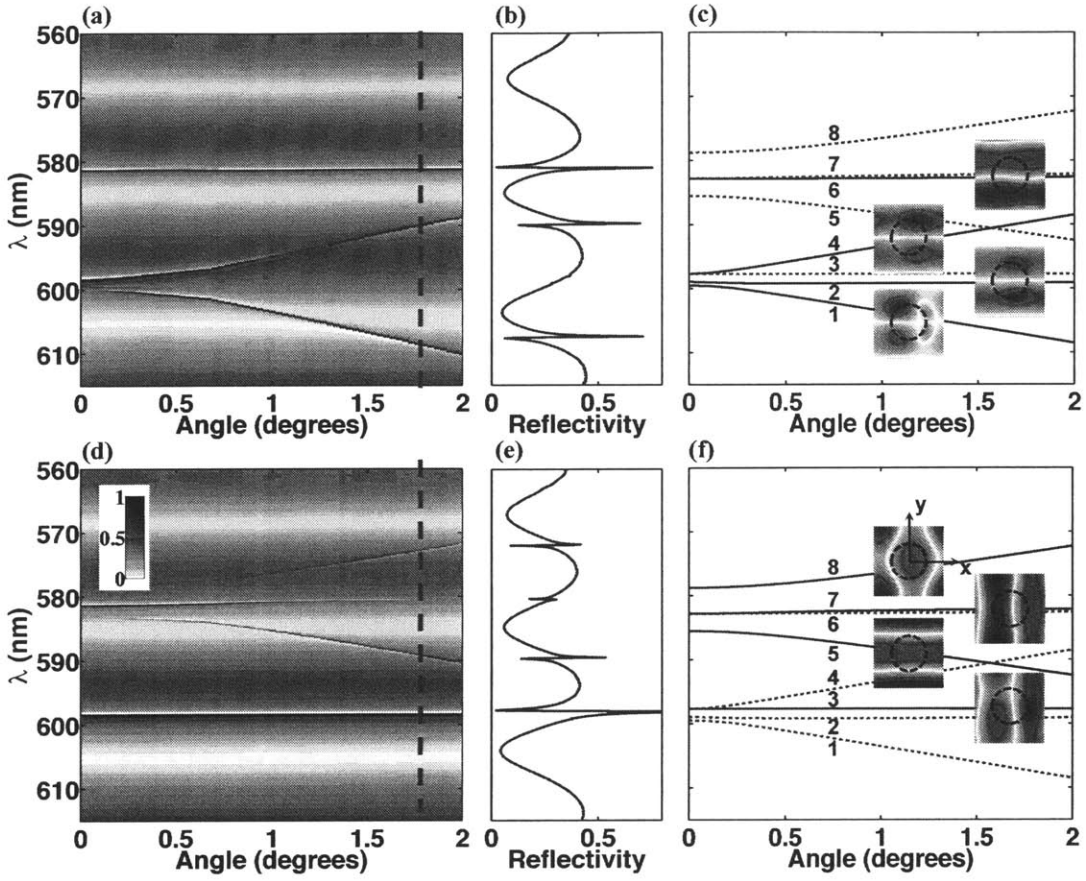

Figure 2-4: Band diagrams of the PhC obtained from reflectivity measurement and finite difference time domain (FDTD) simulation. Reflectivity measurements of the PhC with (a) E_y and (d) E_x polarized beam. (b), (e) A slice of the reflectivity spectrum at 1.8°. (c), (f) Band diagram of the eight lowest energy modes (measured at the Γ point) of the PhC obtained from FDTD simulation. The four lower frequencies modes (numbered 1-4) are TE-like and the four higher frequencies (numbered 5-8) are TM-like. Modes excited externally by odd (even) polarized source with respect to the x-axis are colored purple (green); other modes are shown with gray dashed lines. Their E_z field profiles at the center of the Si_3N_4 layer at $\mathbf{k} = [0.01,\ 0]\cdot(2\pi/a)$ are also shown. Contour of the hole is shown with black dashed circle. The inset depicts a schematic of the unit computational cell used in the numerical calculation. By applying periodic boundary conditions the simulated structure becomes periodically infinite.

the center of the top surface of the 250 nm thick Si_3N_4 layer and was filled with refractive index of n = 1.49 corresponding to toluene. Periodic boundary conditions in the in-plane directions were applied with periodicity set to 320 nm. A schematic drawing of the computational cell is shown in the inset of Fig. 2-4(c). The realization of the infinitely thick layers was achieved by burying the out-of-plane boundaries into perfectly matched layer (PML) [24] while leaving enough space between the PML layer and the Si_3N_4 boundary. In the real structure, the SiO_2 and toluene are each a few micrometers thick making the evanescent tail of the guided resonance field negligible at their outer boundaries, therefore justifying modeling effectively infinitely thick layers in the numerical calculations. We used the Harminv tool of MEEP [23] to calculate the resonant frequencies of the structure and their radiative quality factors.

Fig. 2-4(c) and 2-4(f) show the dispersion curves of the eight lowest energy bands along the Γ-X line ($\mathbf{k}(\Gamma)$ = [0, 0]·(2π/a), $\mathbf{k}$(X) = [0.5, 0]·(2π/a), $\mathbf{k} = [k_x, k_y]$ and k_x = (ω/c)sin(θ)). The four lower frequencies bands are TE-like (numbered 1-4) and the four higher frequencies are TM-like (numbered 5-8). The presented E_z component of all eight modes are calculated at the center of the Si_3N_4 layer at $\mathbf{k}$ = [0.01, 0]·(2π/a). The calculated resonant wavelengths are shifted by not more than ±0.5% from the measured spectra, well within the uncertainty of the measured periodicity or the value of the refractive index. Exception to that is the TE-like mode number 2 in Fig. 2-4(a) that appear to be very faint (almost missing): we explain the cause for this later.

It is evident from the measured spectral reflectivity of Fig. 2-4(a) and 2(d) that the incident beam may excite different modes of the PhC depending on its polarization. This can be understood from symmetry considerations: exciting the PhC slab with a source of one type of symmetry results in coupling to the modes of the same type of symmetry only. Note that moving away from Γ to X the symmetry group changes from C_{4v} to C_{1h} [25], reducing the number of irreducible representations from 5 to 2. Mirror reflection operation around the x-axis leaves the modes of one irreducible representation unchanged, while the modes of the other irreducible representation are altered by a factor of -1. We can determine the symmetry of each mode by examining the mode profile of its E_z component as shown in Fig. 2-4(c) and 2-4(f). Modes 1, 2,

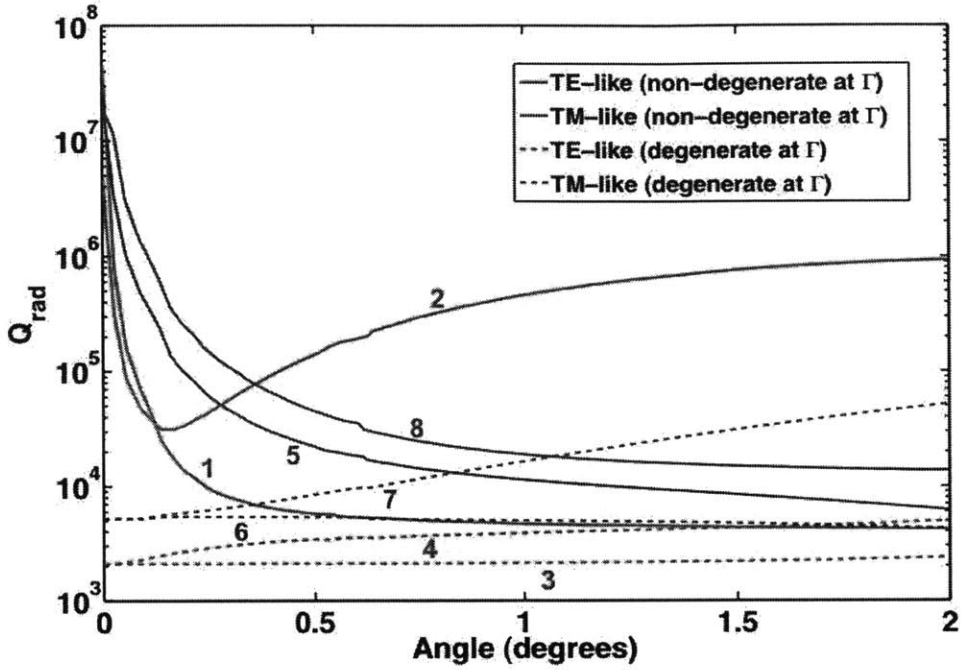

Figure 2-5: Simulation results for radiative quality factors. The high-Q singly-degenerate modes are shown with solid lines, while the doubly-degenerate (at Γ) are shown with dotted lines.

4, and 6 are altered by a factor -1 under mirror reflection operation around the x-axis and hence excited by E_y polarized source, while modes 3, 5, 7, and 8 are unchanged under the same operation and hence excited by E_x polarized source.

Fig. 2-5 depicts the calculated Q_{rad}^{total} of these eight bands. It reveals that while the doubly-degenerate (at Γ) bands 3, 4 and 6, 7 have finite Q_{rad}^{total} at $\mathbf{k}\approx 0$, the singly-degenerate (at Γ) bands 1, 2, 5, and 8 have Q_{rad}^{total} that go to infinity when approaching $\mathbf{k}=0$. This can be qualitatively understood from symmetry arguments. As mentioned earlier, a mode at the Γ point belongs to one of five irreducible representations of the C_{4v} point group [20, 25]. One of the irreducible representations is doubly degenerate and has the same symmetry as free-space modes, while the rest are all singly degenerate and are completely decoupled from free-space modes. As a result, Q_{rad}^{total} of these four singly-degenerate modes at the Γ point should be infinite despite lying within the light cone, while the doubly-degenerate modes have finite Q_{rad}^{total}. As we move

away from Γ to X the point group becomes C_{1h} and doubly-degenerate modes split into two. The two irreducible representations of the C_{1h} point group share symmetry with the free-space modes and therefore Q_{rad}^{total} become finite for all resonances, as is evident from the calculation.

2.5 Temporal coupled-mode theory

To gain a deeper insight into the physics of the measured resonances, we developed a semi-analytical temporal coupled-mode theory model that accounts for the presence of guided leaky resonances in the Si_3N_4 layer [6, 20]. We assumed that the energy of the resonance is allowed to decay exponentially over time into one of the following four channels: (i) far-field radiation into toluene, (ii) far-field radiation into the SiO_2 layer, (iii) material absorption in the Si_3N_4 layer, and (iv) incoherent scattering losses due to fabrication disorder. Coupling into each of these channels can be quantified by correspondingly defining the following quality factors: (i) $Q_{rad}^{tol} = \omega_0 \tau_{rad}^{tol}/2$, (ii) $Q_{rad}^{SiO_2} = \omega_0 \tau_{rad}^{SiO_2}/2$, (iii) $Q_{loss}^{abs} = \omega_0 \tau_{loss}^{abs}/2$, and (iv) $Q_{loss}^{scat} = \omega_0 \tau_{loss}^{scat}/2$, where ω_0 is the resonant frequency in consideration and τ is the lifetime over which the field decays by e^{-1}. As such, the total radiation into the far-field is characterized by $1/Q_{rad}^{total} = 1/Q_{rad}^{tol} + 1/Q_{rad}^{SiO_2}$, while $1/Q_{loss}^{total} = 1/Q_{loss}^{abs} + 1/Q_{loss}^{scat}$ represents the total loss in the system. At 632 nm, using the prism coupling to the Si_3N_4 layer of the bare wafer, $1/Q_{loss}^{abs}$ of the Si_3N_4 layer was measured to be higher than 10^5 (includes scattering losses of the bare wafer). This provides us with an estimate of an upper bound on Q_{loss}^{abs} of the PhC slab; Q_{loss}^{abs} could be lower than that if the surface was contaminated with absorptive material during the fabrication process.

We excited the model with an incident source propagating from the top and impinging onto the Si_3N_4 layer resonant cavity. From first-order perturbation to Maxwell's equation, energy conservation considerations, and neglecting second-order effects, we attained the following expression for the reflectivity of our sample:

$$|r_{PhC}|^2 = \left| r_d - \frac{\gamma_{tol} \cdot (\gamma_{tol} r_d + \gamma_{SiO_2} t_d)}{i(\omega - \omega_0) + \gamma_{tol}^2/2 + \gamma_{SiO_2}^2/2 + 1/\tau_{loss}^{total}} \right|^2 \tag{2.1}$$

r_d and t_d are the complex reflection and transmission coefficients of the sample without the square lattice of cylindrical air holes. γ_{tol} and γ_{SiO2} are the coupling strengths of the resonant mode to the top environment and the SiO_2 layer respectively, and can be related to the quality factors by $\gamma_{SiO_2}^2 = \omega_0/Q_{rad}^{SiO_2}$ and $\gamma_{tol}^2 = \omega_0/Q_{rad}^{tol}$. From Eq. (2.1), it becomes obvious that there exist two temporal pathways: r_d, represents the direct transmission and reflection processes of the uniform stack, and the second term represents the guided resonances excited within the Si_3N_4 layers whose energy leaks into the far-field. It is the superposition of the two physical processes that contribute to the typical narrow Fano line shapes superimposed on a Fabry-Perot-like background that are observed in the reflectivity spectra of Fig. 2-4(b) and 2-4(e).

In order to retrieve the Q^{total} from the measured data, we first fit the smooth background without the narrow line shapes to retrieve r_d and t_d by curve-fitting the measurement results without the Fano resonances to an analytic formula of a homogeneous slab with an effective refractive index [20]. This accounts for the smooth undulating background in the reflectivity spectrum, as can be seen from the fitted blue line in the right inset of Fig. 2-6. Next, Eq. (2.1) is fitted to the desired Fano resonance of the measured data (red circles in the right inset of Fig. 2-6) using nonlinear least squares method to attain the values of γ_{tol}, γ_{SiO_2}, τ_{loss}^{total}, and ω_0. From these fitted values, the corresponding Q^{total} is retrieved by $1/Q^{total} = 1/Q_{rad}^{total} + 1/Q_{loss}^{total}$, where Q_{loss}^{total} includes losses from both material absorption and scattering due to fabrication imperfections.

The results are summarized in Fig. 2-6, with an example of a fitted Fano resonance curve for the data measured at 0.8° of band 5. A complementary approach that also provides further intuitive understanding to calculate the reflection from such structure was proposed by Pottage *et al* [26].

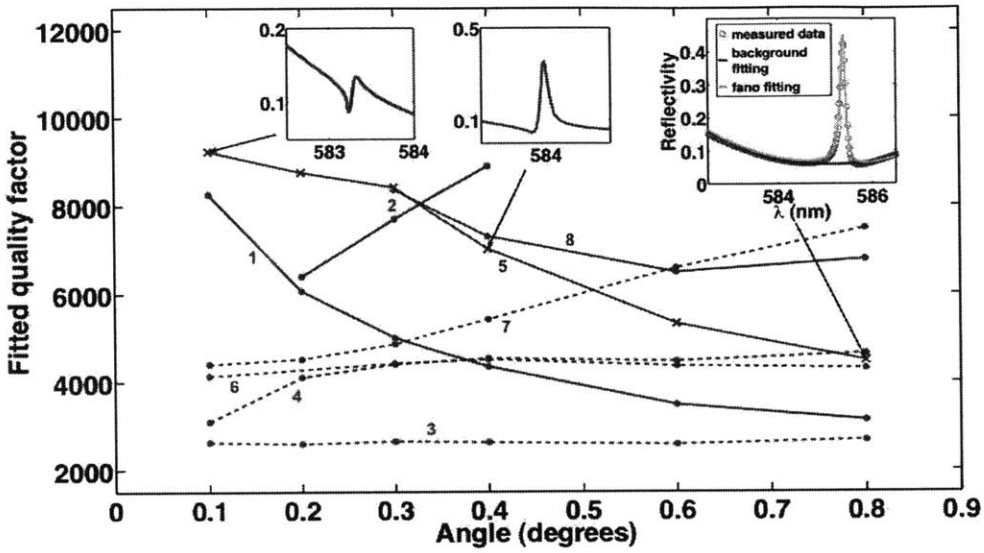

Figure 2-6: Q^{total} values retrieved by fitting Eq. (2.1) to the measured data. Insets show the reflectivity spectra of leaky mode 5 measured at three angles (0.1°, 0.4°, and 0.8°). The right inset depicts an example of the curve fitting process discussed in the text. Note the distinct higher quality factors of the singly-degenerate modes close to zero angle (i.e. zero wave vector).

2.6 Discussion

Fig. 2-6 reveals a clear distinction between the singly-degenerate (modes 1, 2, 5, and 8) and the doubly-degenerate (modes 3, 4, 6 and 7) modes at small angles. While the measured value of Q^{total} increases when approaching $\mathbf{k}$=0 for modes 1, 5, and 8, the doubly-degenerate modes have decreasing or fixed values. We note that although Q^{total} as high as 10^4 are observed, the calculated Q_{rad}^{total} (Fig. 2-5) of the singly-degenerate modes are much greater at small angles, suggesting that close to $\mathbf{k}$=0 the resonant energy decay is dominated by absorption and incoherent scattering from fabrication imperfections ($Q^{total} \approx Q_{loss}^{total} \approx 10^4$), both of which could be significantly reduced by improving the fabrication process. On the other hand, the four low-Q bands 3, 4 and 6, 7 in Fig. 2-6 have Q^{total} values that are comparable to the calculated Q_{rad}^{total} and smaller than Q_{loss}^{total}. Indeed, FDTD calculations of the resonant mode show that the energy confinement is approximately unchanged within the plotted range of angles, suggesting that Q_{loss}^{scat} is relatively constant in the considered range of angles.

Apart from limiting the values of Q^{total} and hence the linewidth of the resonant lineshapes, the presence of relatively large scattering loss and absorption compared to far-field radiation near normal incidence leads to reduced resonant amplitudes. Conversely, the decrease of Q_{rad}^{total} away from the normal provides a better match between Q_{loss}^{scat} and Q_{rad}^{total}, which leads to an increase in the height of the features. This is consistent with Eq. (2.1), and also explains why band 2 appears only weakly in the measurement results shown in Fig. 2-4(a). Unlike other high Q_{rad}^{total} modes whose values decrease rapidly away from the Γ point, the Q_{rad}^{total} of the missing TE-like band 2 remains high (Fig. 2-5) for most angles, resulting in small reflectivity amplitudes which are harder to detect.

2.7 Concluding remarks

In conclusion, we experimentally differentiate and demonstrate the existence of a special class of resonances in PhCs with quality factors that could, in principle, approach infinity despite lying within the light cone. These *non-degenerate* Fano resonances are delocalized modes that decouple from the light cone states at k=0 due to symmetry considerations. A clear distinction between these modes and *degenerate* Fano resonances with finite Q^{total} at the Γ point is presented. With future improved fabrication that decreases the roughness and non-uniformities of the PhC slab, the current observed quality factors of $\sim 10^4$ can be significantly enhanced. The experimental realization of this mode has several important consequences: 1) the strongly enhanced field close to the PhC surface and *the simple access* to it provides a new platform for the study of light and matter interaction; 2) it offers an easy-to-fabricate structure that supports delocalized modes with ultrahigh quality factors; 3) it can be shown from coupled mode theory [27] that up to 50% of external radiation can be coupled to these strongly confined modes in symmetric PhC slabs, when one ensures that the Q-matching condition between the radiative life-time, and the absorptive life-time is satisfied; and 4) despite the macroscopically large area resonator, only a few high-Q modes are supported within a fairly broad frequency range. The delocalized

nature of this mode is particularly important in applications where the interaction of an enhanced electric field with a macroscopic volume of matter can dramatically improve the performance of the process, such as in bimolecular sensing and organic light emitting devices. Furthermore, the realization of this novel resonance could enable the enhancement and the demonstration of new physical phenomena in laser physics, energy conversion, nonlinear optics, and optical filters.

Chapter 3

Fabricating centimeter-scale high quality factor two-dimensional periodic photonic crystal slabs

3.1 Introduction

High quality factor (Q) micro-resonators [28, 29], characterized by narrow resonance linewidths and long photon storage time, are excellent candidates for sensors with enhanced detection sensitivity [30, 31] and efficient large-area laser cavities [32, 33]. In such practical device applications, it is desirable to realize high Q resonators with simultaneously large areas and wide free spectral ranges (FSRs). Cavities with large areas are desirable to trap sufficient energy for realizing sensing and energy harvesting. In addition, a wide FSR ensures that adjacent discrete cavity modes are well separated in order to promote single-mode operation. Several very high Q micro-resonators such as defects in photonic crystals (PhCs) [32–35], micro-toroids [30,31,36], and micro-ring resonators [37, 38] have been extensively studied over the past few decades. However, defect PhC devices have very small sizes, and while micro-toroids and rings are typically larger, their FSRs are fairly narrow. Here, we demonstrate optimized fabrication of a centimeter scale 2D defect-free PhC through which we obtained increased Q by

a factor of three compared to [1]. Thus, the final samples possess high Q, large area, and wide FSR. By analyzing the resonances of our structure through reflectivity measurement over a broad frequency range, the pattern quality was quantified in terms of Q. This Q reflects not only the surface roughness and pattern shape, but also the sidewall roughness and the nanometer scale variation of the pattern properties over the whole structure, such as periodicity and hole sizes. Therefore, Q can systemically quantify the average quality of millions of periodic patterns over a centimeter scale, which is not feasible to do by characterizing a localized nanometer scale area with atomic force microscopy (AFM) or scanning electron microscope (SEM).

3.2 Sample fabrication

To achieve high Q resonances in the visible wavelength range, both the bulk material properties and the nanoscale geometry have to be considered. Experimentally attainable Q is bounded by bulk material absorption. A LPCVD-deposited Si_3N_4 layer on top of a 6 μm thick SiO_2 layer on Si substrate is used in this study. Through an absorption test enabled by a prism coupler, Q limited by bulk materials absorption is found to be 5×10^5 at $\lambda = 633$ nm. With a refractive index of 2.02, Si_3N_4 forms sufficient index contrast with SiO_2 (index of 1.45) below and air or fluids on top, so more than 80% of the mode energy is confined within this Si_3N_4 layer with thickness of less than 200nm. The fabrication process consists of deposition of a quadlayer resist stack, pattern definition by interference lithography (IL) [39], pattern transfer by reactive ion etching (RIE), and removal of the remaining resist. Fig. 3-1 shows the schematic outline of the fabrication process. The quadlayer is comprised of a layer of antireflection coating (ARC, XHRiC-16), a thin layer of SiO_2 deposited by electron beam evaporation, a negative photoresist (PR, THMR-iN PS-4), and another thin layer of ARC (ARC′, XHRiC-16). XHRiC-16 is an ARC material specifically designed for dry etching processes, which makes metal hard masks unnecessary. Metal hard masks are robust, but even a very small amount of metal residue substantially increases light absorption and therefore limits the highest achievable Q's. XHRiC-16

is robust enough to etch several hundred nanometers of Si_3N_4 and eliminates any potential metal contamination. ARC is introduced to limit the amount of light reflected back into the PR layer. Otherwise, this reflected light will form a vertical standing wave with the incident light, which causes poor sidewall profiles in the PR layer. The thickness of the ARC layer is optimized to minimize the reflection at the bottom of the PR layer. Together with another thin layer of ARC (ARC′) on top of the PR layer, the reflection can be further reduced, as shown in Fig. 3-1(e). It reduces the overall reflection by roughly a factor of two and the minimum reflection by a factor of one hundred, which provides tolerance to an increase in reflectivity from a small deviation in the thickness of each layer of the resist stack. The SiO_2 layer is used as a hard mask while the ARC layer is etched.

After the deposition of the resist stack, IL uses a 325 nm He/Cd laser to define the 2D periodic pattern on the PR layer. The laser beam is split into two mutually coherent beams, and the angle between the two beams determines the periodicity of the pattern. A single exposure defines a 1D grating pattern, and a following perpendicular exposure defines the 2D square array pattern [40]. The shape and the size of the holes after development are determined by the exposure time. Short exposure results in large diamond shape holes, and long exposure results in small circular shape holes. Optimal exposure typically produces round holes with a diameter to periodicity ratio (d/a) of 0.3-0.5. The ratio, d/a, is 0.5 in this study. Two types of IL systems are explored here: Lloyd's mirror (LM) and Mach-Zehnder (MZ) [41]. Higher Q's were observed from the samples exposed using MZ. The comparison between the two IL systems will be further discussed in a later section. The exposed PR is hard baked (110 °C, 90 sec) and developed in a commercial developer CD-26 (20 °C, 60 sec). The image of a 4-inch wafer after development is shown in Fig. 3-2(b). The 2D periodic pattern on the PR layer produced a diffraction pattern when two external fiber light beams illuminating it. Then, the PR pattern is transferred to the Si_3N_4 layer using RIE (Plasmatherm 790). The two ARC layers are etched with $He:O_2$ = 16:8 sccm (10 mTorr, 200 V), and SiO_2 and Si_3N_4 are etched with $CHF_3:O_2$ = 16:3 sccm (10 mTorr, 400 V). After the RIE steps, the remaining ARC layer is removed

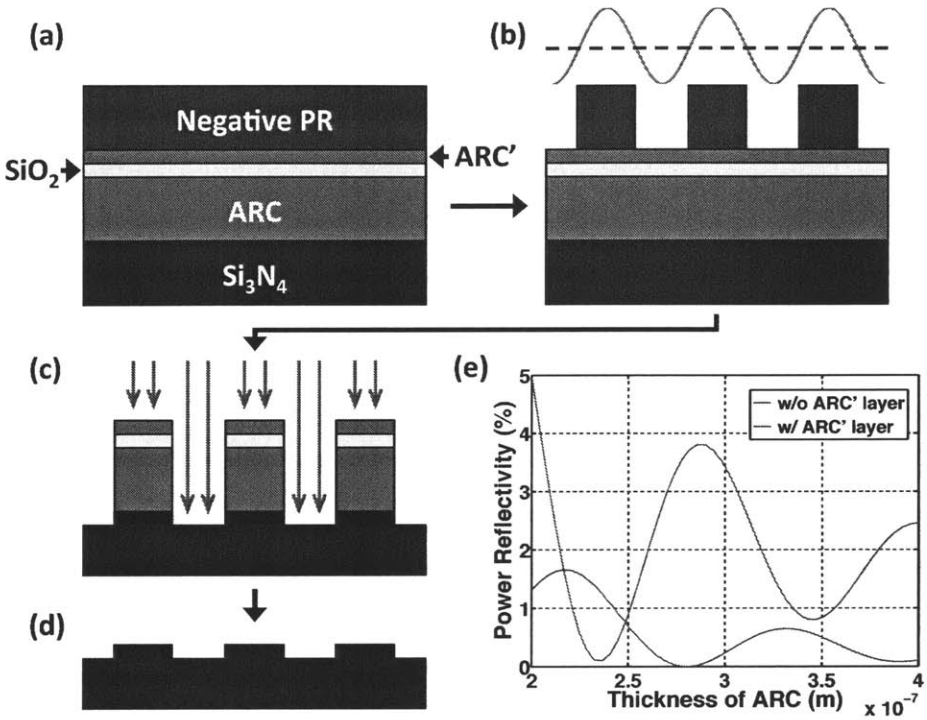

Figure 3-1: (a)-(d) Schematic outline of the process flow: (a) Deposition of the resist layers, where ARC′ stands for a thin ARC layer, (b) pattern definition by interference lithography followed by development, (c) pattern transfer to the Si_3N_4 layer by RIE, (d) removal of remaining resist stack. (e) Reflectivity at the bottom of the PR layer as a function of the thickness of the ARC layer. It is important to minimize the amount of light reflected back into the PR layer because it forms a vertical standing wave with the incident light. This produces poor sidewall profiles after development, and hence low Q's of resonances. The green and red curves represent the reflectivity with and without 45 nm of ARC′ layer, respectively. The existence of the ARC′ layer reduced overall reflectivity by roughly half and so did the minimum reflectivity by a factor of one hundred.

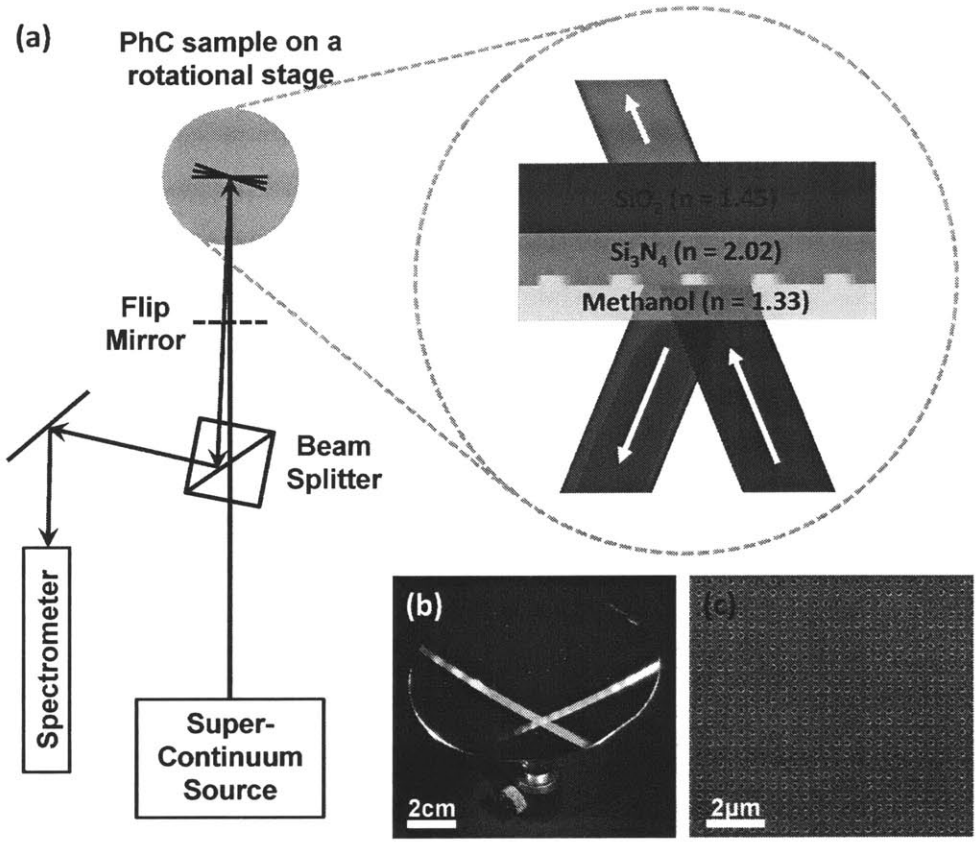

Figure 3-2: (a) Schematic drawing of the reflectivity measurement setup. Enlarged view of reflection path of light from the PhC sample is also represented on the right. (b) Image of an exposed 4-inch wafer after development. The two diffraction beams were produced by two fiber light beams. This shows the 2D periodic pattern was defined over the entire area of the wafer. (c) Top-view scanning electron micrograph of the final sample with periodicity of 375 nm.

completely by immersion into a commercial post-etch residue remover EKC-265. A top-view SEM image of the final PhC structure is shown in Fig. 3-2(c). Higher Q's were observed when the PR after development is descummed using O_2 RIE. This descumming step smoothens the wavy sidewalls of the PR pattern, allowing more anisotropic pattern transfer afterwards. This step will be further discussed in a later section.

3.2.1 Interference lithography

IL is the most important step that defines the periodicity and the shape of the holes. IL has many benefits compared to the conventional photolithography. First of all, it doesn't require a photo mask. Therefore, you don't have to spend time making a photo mask, and your pattern is not limited by the feature size of the photo mask. Second, it is very quick (order of a few minutes) and generates dense features over a wide area (order of cm^2) without loss of focus. In 1 cm^2 area, around one billion holes are be defined in only a few minutes, while it takes tens of hours to generate the same number of patterns with an e-beam lithography. The smallest feature size that IL can make is half of the wavelength of the beam, so with UV lasers a pattern with a feature size as small as few hundreds of nm can be produced. The drawback of IL is that the shape of the pattern it can make is very limited. You cannot make an arbitrary pattern with IL. A single exposure can make a 1D grating, and a double exposure can make a 2D square array of cylindrical pattern. Using more than one beam can make hexagonal array patterns, but still there is limited freedom in pattern shape.

An illustration of the Lloyd's mirror IL system is shown in Fig. 3-3. The source is a 325 nm He/Cd laser. Consider the two large-area monochromatic plane waves of wavelength λ and amplitudes E_1 and E_2, as shown in Fig. 3-3(b). Two waves can be represented as

$$\mathbf{E}_1(r,t) = \hat{e_1} E_1 cos[\mathbf{k}_1 \cdot \mathbf{r} - \omega t + \phi_1(t)] \tag{3.1}$$

$$\mathbf{E}_2(r,t) = \hat{e_2} E_2 cos[\mathbf{k}_2 \cdot \mathbf{r} - \omega t + \phi_2(t)] \tag{3.2}$$

where $\phi_1(t)$ and $\phi_2(t)$ are reference phases of each beam. The combined field amplitude at $\mathbf{r}$ is $\mathbf{E} = \mathbf{E_1} + \mathbf{E_2}$, and thus the intensity of the interference pattern is given by

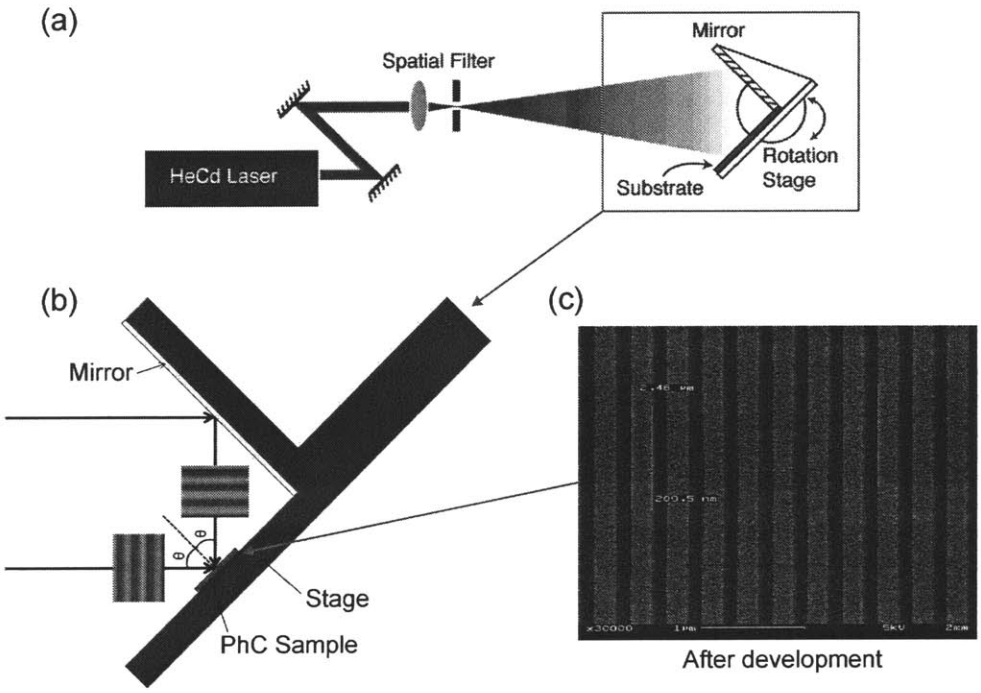

Figure 3-3: (a) Diagram of the Llyod's mirror setup. Since the beam is split at the mirror, path difference of two beams is minimized, so the pattern becomes less vulnerable to vibration. (b) Magnified diagram of the stage. The angle of incidence is controlled by rotating the stage. (c) A 1D grating pattern defined on PR after a single exposure.

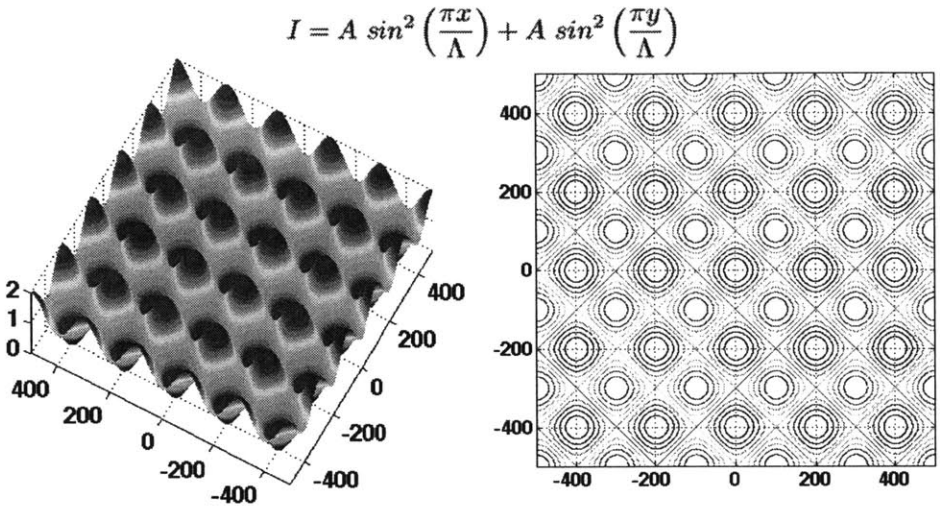

Figure 3-4: Field intensity distribution after double exposures and its contour diagram

$$
\begin{aligned}
I(\mathbf{r}) &\propto < |\mathbf{E}_1(\mathbf{r},t)|^2 > + < |\mathbf{E}_2(\mathbf{r},t)|^2 > + 2 \cdot < \mathbf{E}_1(\mathbf{r},t) \cdot \mathbf{E}_2(\mathbf{r},t) > \\
&= E_1^2/2 + E_2^2/2 + < (\hat{e_1} \cdot \hat{e_2}) E_1 E_2 cos[(\mathbf{k}_1 - \mathbf{k}_2) \cdot \mathbf{r} + \phi_1(t) - \phi_2(t)] > \\
&= E_1^2/2 + E_2^2/2 + < (\hat{e_1} \cdot \hat{e_2}) > E_1 E_2 < cos[(\mathbf{k}_1 - \mathbf{k}_2) \cdot \mathbf{r} + \phi_1(t) - \phi_2(t)] > .
\end{aligned}
\tag{3.3}
$$

As can be seen in Eq. (3.3), there are two conditions to be satisfied for a stable interference pattern: i) $< (\hat{e_1} \cdot \hat{e_2}) > \neq 0$ and ii) $\phi_1(t) - \phi_2(t)$ is stationary. Therefore, two beams have to be mutually coherent and their polarization direction must not be orthogonal. Solving the cosine term gives the period of the pattern, $\Lambda = \lambda / 2 sin\theta$. Path difference is minimal in this setup, and its relatively long coherence length compared to the path difference ensures the mutual coherence condition.

A single exposure defines a 1D grating pattern, as shown in Fig. 3-3(c). A double exposure with the second exposure after rotating the sample by 90° defines a 2D square array pattern on the PR layer. The shape of the pattern depends on the exposure time and the type of PR, and it is illustrated in Fig. 3-4 and 3-5. Fig. 3-4 shows that the contour changes from circular (red) to diamond (green) to circular (blue). A negative PR is a type of PR which becomes insoluble after it is exposed to

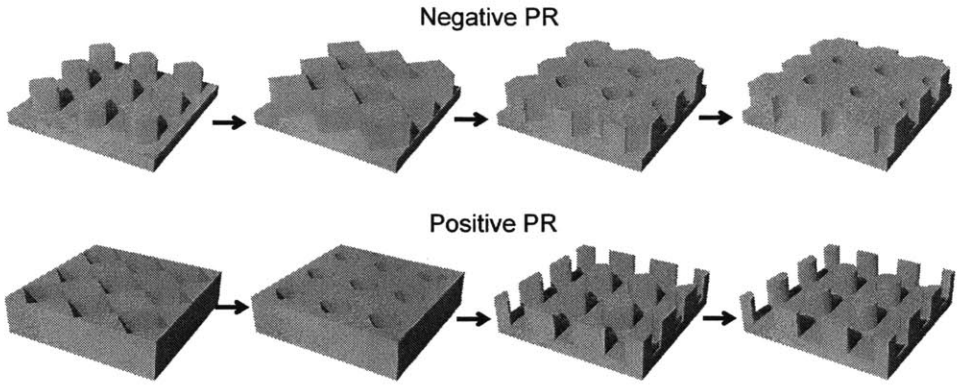

Figure 3-5: Illustration showing how the pattern on a negative and a positive PR change with exposure time. For a negative PR, the pattern changes from the rods to the holes. Cylindrical rods initially appear at maximum intensity points, and the insoluble area expands and meets as exposure time increases, and finally leaves holes. Near the saddle point, the pattern becomes a diamond shape.

light. Therefore, with very short amount of exposure, the area around the maximum intensity (red) becomes insoluble first, so cylindrical rods are made. As exposure time increases, the insoluble area expands, and the cylindrical rods become diamond (green) rods, and finally the rods meet each other and leaves cylindrical (blue) holes. This process is illustrated in Fig. 3-5 for both types of PR. Theoretically, either type of PR can produce both cylindrical rods and holes. However, too short exposure time produces lots of noise, and the resulting pattern rarely has high quality. Therefore, a negative (positive) PR should be used for holes (rods). With right amount of exposure, a 2D square array of cylindrical hole pattern can be obtained from a negative PR. A reasonably circular pattern has size of $d/a \approx 0.3 \sim 0.5$, which can be controlled by exposure time. To get a larger ($d/a > 0.5$) hole, you need to use Asher (isotropic dry etching machine) to expand the holes after development.

Mach-Zehnder (Fig. 3-6) is the other type of IL system. MZ shares exactly the same principle, but it generally produces better patterns at the cost of complexity of system alignment. Two most notable strengths of MZ are 1) stable exposure and 2) larger exposure area. MZ has a piezo sensor which detects even very small vibrations and move the beam-splitter stage to compensate the vibrations. MZ has much longer arm length than LM, which enables larger exposure area.

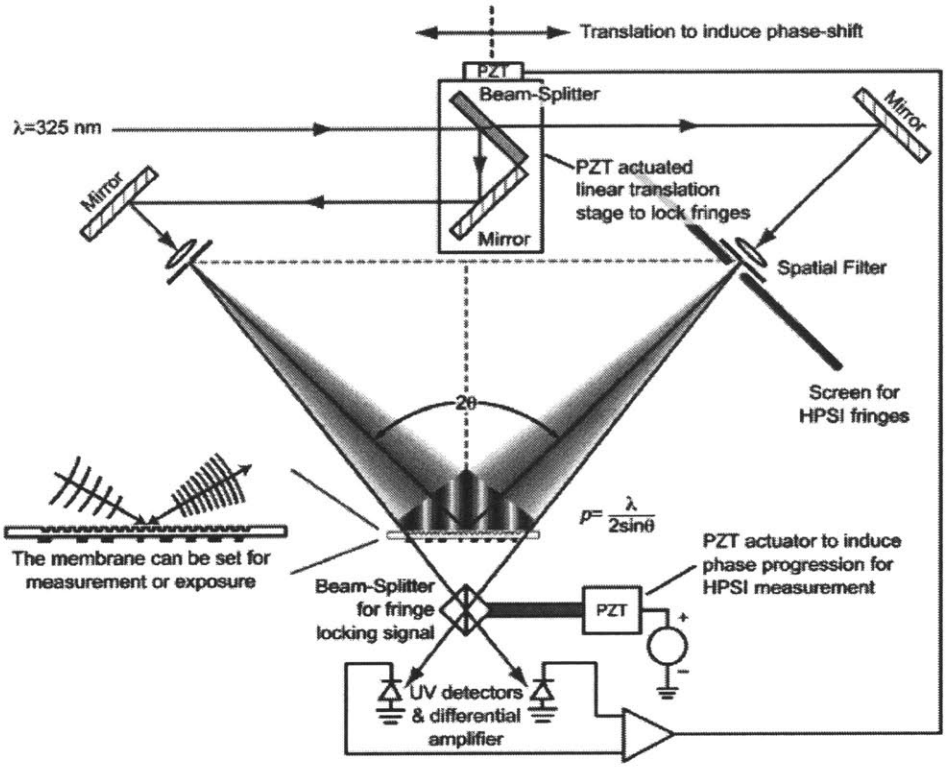

Figure 3-6: Diagram of the Mach-Zehnder setup. Llyod's mirror and Mach-Zehnder share the same principle: formation of a standing wave with two mutually coherent laser beams. Compared to Lloyd's mirror, Mach-Zehnder produces more stable pattern since it has a piezo sensor which recognizes and minimizes even very small vibrations from the environment.

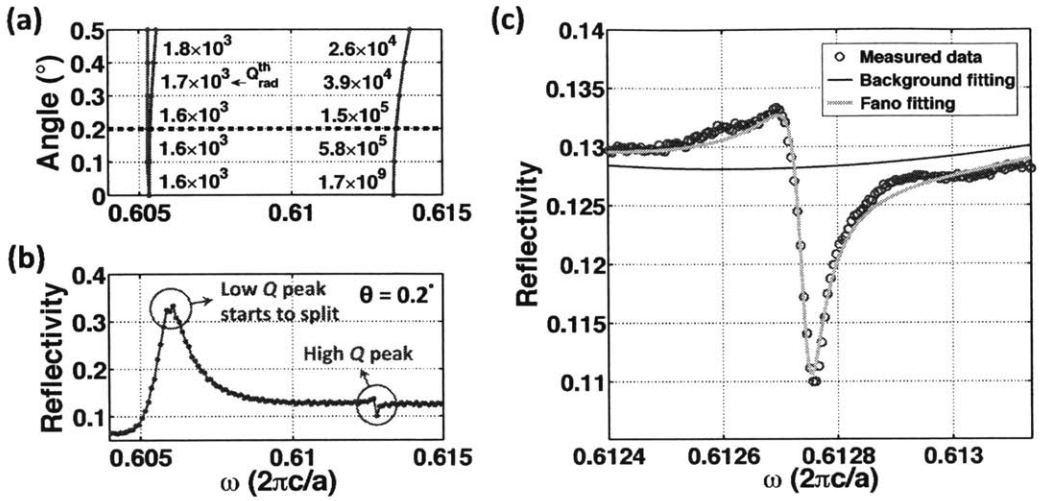

Figure 3-7: (a) The band diagram calculated with MEEP. The frequency is plotted along the x-axis, and the wave vector is converted to the angle and plotted along the y-axis. The numbers inside the graph ($Q^{\text{th}}_{\text{rad}}$) represent the theoretical radiative quality factors of each mode calculated with MEEP. The two lines on the left are low Q modes degenerated at the Γ point, and the line on the right is a high Q mode whose radiative Q diverges at the Γ point. (b) Experimental reflectivity data measured at 0.2°. The frequencies of the peaks agree well with the calculation result. (c) The high Q peak in (b) was measured again with a higher resolution, and the data was fitted to the reflectivity formula derived from coupled mode theory. The red dots are the measured data, the blue curve is the fitted background, and the green curve is the final fitting result.

3.3 Sample characterization

The characterization of the PhC slab is performed when the light from a supercontinuum laser source (SuperK Compact, NKT Photonics) is reflected from the sample, and this light is recorded with a high resolution scanning monochromator (1250M, HORIBA) at small incident angles (0-0.5°). The measurement setup is illustrated in Fig. 3-2(a). The sample was placed in a precision demountable liquid cell containing methanol, and the whole cell was mounted on a motorized rotational stage (ESP300, Newport). To corroborate experimental results, finite difference time domain simulation, MEEP [23], was performed to calculate the modes of the PhC. Figs. 3(a) and 3(b) show the simulation and the experimental results, respectively.

Fig. 3-7(a) is the band diagram of the PhC. Wave vector $\boldsymbol{k}$ is converted to

angles on the y-axis while the frequency is represented by the x-axis. Calculated Q_{rad} of each mode is also shown in the plot. The singly degenerate mode has infinite Q_{rad} at Γ, while the doubly degenerate mode has finite Q_{rad} at Γ and split into two modes as $\boldsymbol{k}$-point moves away from Γ towards X [1]. Fig. 3-7(b) is the reflectivity measurement result at $\theta = 0.2°$. In Fig. 3-7(a), the doubly degenerate mode starts to split at $\theta = 0.2°$, and this was experimentally observed, as shown in Fig. 3-7(b). Also, the spacing between the doubly degenerate (or low Q) mode and the singly degenerate (or high Q) Fano resonant mode in Fig. 3-7(a) and the one in Fig. 3-7(b) agree well with each other. As the reflectivity measurement approaches $\theta = 0°$, the observed Q^{total} (where $1/Q^{\text{total}} = 1/Q_{\text{rad}} + 1/Q_{\text{loss}}$) of a high Q Fano resonant mode can be approximated to be the same as Q_{loss}. In this way, the degree of fabrication imperfections was quantified in terms of Q^{total}. This is a valid approximation because Q_{rad} of the high Q mode diverges as $\boldsymbol{k}$-point moves toward Γ, while Q_{loss} was found to be almost constant [1]. The sidewall roughness and variations in periodicity and size of holes are taken into account in the Q^{total}, as well as the surface roughness and pattern shape. Therefore, this approach enables measurement of the average quality of overall PhC structure, while the common visual analysis tools such as AFM or SEM provide quantitative descriptions of microstructure details. Note that, however, the exact origin of Q_{loss} is hard to trace using this approach.

Q^{total} of the sample is retrieved by fitting Eq. (3.4) to the reflectivity measurement data. This formula has previously been derived from temporal coupled mode theory [1].

$$|r_{\text{PhC}}|^2 = \left| r_d - \frac{\gamma_t \cdot (\gamma_t r_d + \gamma_b t_d)}{i(\omega - \omega_0) + \gamma_t^2/2 + \gamma_b^2/2 + 1/\tau_{\text{loss}}} \right|^2 \tag{3.4}$$

r_d and t_d are the complex reflection and transmission coefficients of the sample without the 2D pattern, which can be obtained by fitting the background data (Blue line). γ_t and γ_b are the coupling strengths of the resonant mode to the top (Methanol) and the bottom (SiO_2) layers, respectively. ω_0 and $1/\tau_{\text{loss}}$ are center frequency of the resonance and resonant energy decay rate due to fabrication imperfections. These

Table 3.1: Fitted Q^{total} of various PhC samples.

Q^{total}	Hole Depth		
	60nm	120nm	180nm
LM	10K	O(10^3)	O(10^2)
MZ	16K	14K	9K
Optimized MZ	32K	19K	17K
E-beam lithography	10K	7K	6K

four parameters are fitted using a non-linear least squares method (Green line) and used to compute Q^{total}. The fitting process is shown Fig. 3-7(c). Table 3.1 shows Q^{total} obtained from PhC slabs fabricated with various methods and hole depth. The thickness of Si_3N_4 layer was 180 nm, and holes were etched 60, 120, and 180 nm. In general, deeper hole depths resulted in lower Q because of longer RIE step.

3.4 Discussion

IL is a fast, inexpensive, and maskless lithography method; therefore, it is an optimal choice to fabricate large area periodic patterns. We studied two IL systems: LM and MZ [41]. Both systems share the same principle: formation of a standing wave with two mutually coherent laser beams. The MZ setup has a piezo sensor which recognizes and minimizes even very small vibrations. MZ can also expose larger size substrates. As shown in Fig. 3-2(b), the entire 4-inch wafer can be exposed with a single exposure. Therefore, it provides a high throughput as well as ease of quality control. Since all samples produced from the same exposure have the same degree of exposure quality, we were able to determine whether Q measured from the PhC is attributed to the exposure or other factors. In contrast, in the LM setup, each piece has to be exposed one by one, resulting in varying degree of exposure quality. In table 3.1, PhCs fabricated from LM showed Q of 10K [1], but the ones from MZ (other conditions were not changed) showed Q of 16K. As shown in Fig. 3-8(a), PR sidewalls were wavy and not perfectly vertical after development. Common positive PRs that do not cross-link may be heated up to their softening point and reflowed. However, because most negative PRs (including THMR-iN PS-4) cross-link, they cannot be

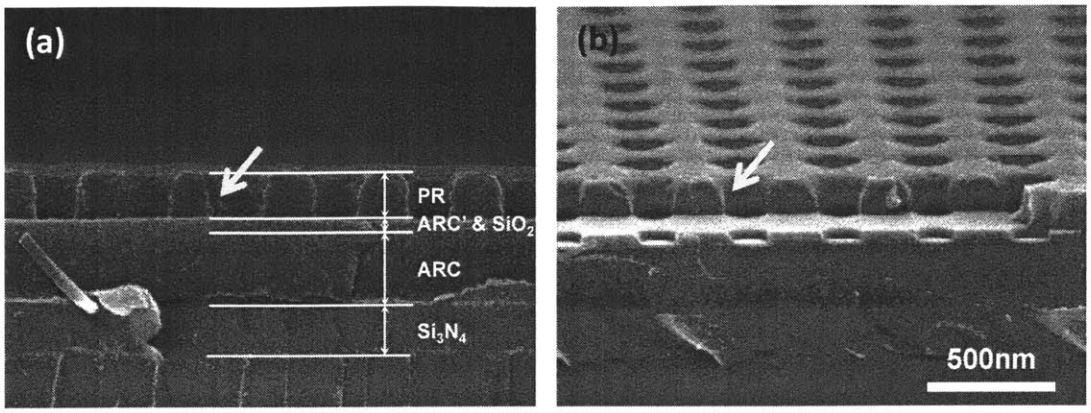

Figure 3-8: (a) After development, sidewall profiles were wavy and slanted. (b) After O_2 RIE process, sidewall profiles became more vertical and straight.

smoothened out through a reflow process. Therefore, O_2 RIE was used to make the sidewalls of the PR layer more even and vertical, as shown in Fig. 3-8(b) [42]. This allows more anisotropic etching in the subsequent layers. Improvements in the Q's were observed when this step was implemented. This O_2 RIE etches the ARC′ layer at the same time. Different gas compositions for SiO_2 and Si_3N_4 RIE were also studied. We confirmed that the mixture of CHF_3:O_2 = 16:3 results in higher Q than CF_4 gas [37]. After all of these optimization steps, Q of 32K was measured.

Lastly, we fabricated PhC slabs using electron beam lithography (F-125, Elionix). The pattern area was 600×600 μm^2, which is sufficiently large that Q is not limited by its pattern size [17]. Exposure took around 6 hours, but their Q's were not higher than the ones fabricated using IL. By optimizing exposure conditions, Q can be further improved, but the low throughput and limited pattern area prevents electron beam lithography from being considered as the optimal candidate for large area high Q PhC fabrication.

3.5 Concluding remarks

In conclusion, we reported a centimeter scale large-area high-Q defect-free 2D PhC fabrication process and a unique way to measure and comprehensively quantify the quality of 2D PhC slabs. The fabrication steps that we established here improved Q

by a factor of three from our previous study [1]. We further confirmed that IL is a more suitable method to fabricate macroscopically large PhCs in terms of cost and time efficiency, compared to e-beam lithography. Since theoretical $Q_{\mathrm{rad}}^{\mathrm{total}}$ is unbounded, improving the fabrication process can further enhance attainable Q in the future. For example, by expanding the IL laser beams to a wider angle or by shaping the beam profile to a more uniform distribution, spatial power distribution will become uniform, and spatial variation of the pattern will be decreased. Post-process thin dielectric film coating using atomic layer deposition might also improve Q [43]. Furthermore, the fabrication and measurement schemes presented here can be universally used for other materials or structures. Along with the fact that the 2D pattern studied here has ultra high Q, large area, strong confinement near its surface, and ease of incorporating into a system, this work could be utilized to realize biomolecular sensors, organic light emitting devices, large area lasers, and other energy conversion systems.

Chapter 4

Terahertz lasing action in high-pressure optically-pumped molecular gases

4.1 Introduction

Optically-pumped far-infrared (OPFIR) molecular gas lasers, which operate through a rotational state population inversion induced by an infrared (IR) pump laser, remain a powerful source of terahertz (THz) radiation [44–46]. Commercially available OPFIR lasers are typically huge (1-3 m long $\times$ 2 cm radius) because of their low-pressure operation and the need to absorb pump power [45–48]. Various models have been developed to explain the behavior of OPFIR lasers, whose primary inversion occurs between two rotational states in an excited vibrational level of the molecule. [44–46]. Later, a significantly improved theoretical framework was introduced to describe the spatio-temporal dynamics of OPFIR lasers by considering both spatial diffusion and collisional processes to estimate radial population gradients and overlap of the inversion and the various cavity modes [49]. The results of that model agreed quite well with the experimentally measured low-pressure behaviors and allowed the net effective gain to be predicted accurately.

However, Ref. [50] demonstrated an OPFIR laser more than 1,000 times smaller, and it was experimentally observed that this compact laser operated at much higher pressures than could be explained by these models. High-pressure operation provides power and frequency tunability, but a high pressure limit - or cutoff pressure - is reached through a mechanism called the vibrational bottleneck. Since the primary relaxation channel for pump-induced vibrational excitation is diffusion to and collision with the cell walls, vibrationally-excited molecules become increasingly trapped there as pressure increases. Consequently, as the rotational levels fill at high pressure, the pump-induced inversion is quenched. Applying existing models of OPFIR laser performance to the compact, 0.25 cm diameter laser cavity incorrectly predicted that the vibrational bottleneck would occur at a cutoff pressure of 0.44 Torr, independent of pump power [50]. However, the experiment showed lasing up to 1.7 Torr with a cutoff pressure that increased with increasing pump power.

Through subsequent analysis of the collisional energy transfer, it was found that high-lying vibrational levels become increasingly important to the operation of the laser [50–56]. Indeed, this vibrational excitation collisionally redistributes molecules to higher levels in a manner that depends on the pump rate, explaining the pump power-dependent cutoff pressure observed. However, to our knowledge, no physical model of this high pressure performance has been developed that adequately describes the increasing role these excited vibrational levels play.

Here, we expand the theoretical framework of Ref. [49] and provide new experimental data to describe for the first time how the excited vibrational levels contribute to high-pressure operation of compact OPFIR lasers. The new model addresses the three main limitations of previous models. First, a detailed calculation of the dynamically evolving pump rate is developed. Second, a detailed diffusion model for the wall collision rate is derived in order to estimate spatial population gradients. Third, a faithful representation of how high-lying vibrational energy levels contribute to the high pressure operation is constructed in spite of the fact that the salient collisional energy transfer rates to these levels are unknown. The pump rate involves many dynamical elements that evolve as the various energy transfer pathways operate, in-

cluding spectral hole burning, saturation, varying pump power absorption length, and radial field and population distributions. The diffusive wall collision rate is rigorously derived from first principles, and the methodology for involving high-lying vibrational energy level system is made to reflect the fact that an increasing number of vibrational levels are involved as pressure and pump power increase. Combining these elements, we present a redesigned OPFIR laser model that qualitatively and quantitatively reproduces new experimentally-measured high-pressure behavior for two rotational inversions observed in the popular OPFIR laser gas $^{13}CH_3F$. However, the model can be universally applied to any OPFIR laser gas. In this work, we use $^{13}CH_3F$ in a cylindrical copper cavity (radius $R = 0.25$ cm and length $L_{cell} = 15$ cm) as a prototypical example to simplify the discussion and notation.

The theoretical analysis presented in this paper accounts for OPFIR lasing action in the high-pressure regime while more accurately describing lasing action in the low-pressure regime. Section 4.2 describes the concept of a thermal pool and how it simplifies numerical simulation of the system. Section 4.3 elaborates the pump rate definition, and Section 4.4 derives the wall collision rate. Section 4.5 presents newly measured experimental results. Section 4.6 shows the limitation of the basic energy system presented in Section 4.2, and Section 4.7 introduces a more accurate vibrational energy level system that can be used for high-pressure operation.

4.2 Thermal Pool

The THz lasing action of a polyatomic molecular gas excited by a narrow-linewidth and line-tunable IR CO_2 laser is modeled in this paper. The model considers the ^{13}C isotopomer of methyl fluoride, $^{13}CH_3F$, as a gain medium. Without any simplifications, the rotational and vibrational energy levels of $^{13}CH_3F$ and collisional energy transfer mechanisms among them are very complicated to be modeled accurately. A collisional process, where a molecule in a rotational state i collides with another molecule and changes to a rotational state j as a result, can be expressed as:

$$M_i \xrightarrow{k_{i,j}} M_j \quad \forall i,j \in [1\,,n] \tag{4.1}$$

If there are n states that are thermally populated, then $n^2/2$ collisional rate constants ($k_{i,j}$) are needed to describe energy transfer pathways connecting all rotational states (divided by two due to detailed balance). Considering there are approximately $n \sim$ 3,000 thermally populated states for $^{13}CH_3F$ at $T = 300$K, there are $n^2/2 \sim 4.5 \times 10^6$ rate constants, most of which are unknown. Fortunately, it was found experimentally that the vast majority of rotational states in a vibrational level remains in rotational equilibrium among themselves; consequently, these rotational states may be collectively represented as a "thermal pool" [51, 57–59]. The total population of the thermal pools may evolve in time through the flow of energy governed by the collisional and diffusive processes. A thermal pool can thus be regarded as a collection of rotational states that are in thermal equilibrium, so the relative population of rotational states separated by ΔE are populated according to a Boltzmann distribution ($N_i/N_j = \exp(-\Delta E/k_B T)$) at the operating temperature $T = 300$K. This thermal pool concept enables consolidation of numerous rotational states into a very small number of thermal pools, enabling one to account for many rotational states with only a few easily measured rate constants. The thermal pool concept has been introduced in several OPFIR laser models [51, 57], and was validated by extensive double resonance measurements [52, 56].

Fig. 4-1 illustrates the six lowest vibrational energy levels of $^{13}CH_3F$ and the various energy transfer mechanisms among the rotational and vibrational levels initially considered in this work. The six vibrational levels are: V_0 (ground), V_3, V_6, $2V_3$, V_3+V_6, and $2V_6$ [60]. In methyl halides, each vibrational level is further split into two thermal pools, one for each symmetry type (A and E) that represents the effectively immutable symmetry associated with the nuclear spin alignment of the three H nuclei. Before pumping the gas, these vibrational levels can simply be modeled as thermal pools because all rotational states in the vibrational levels are in rotational equilibrium. However, upon pumping, the rotational states in V_0 and V_3 that are directly

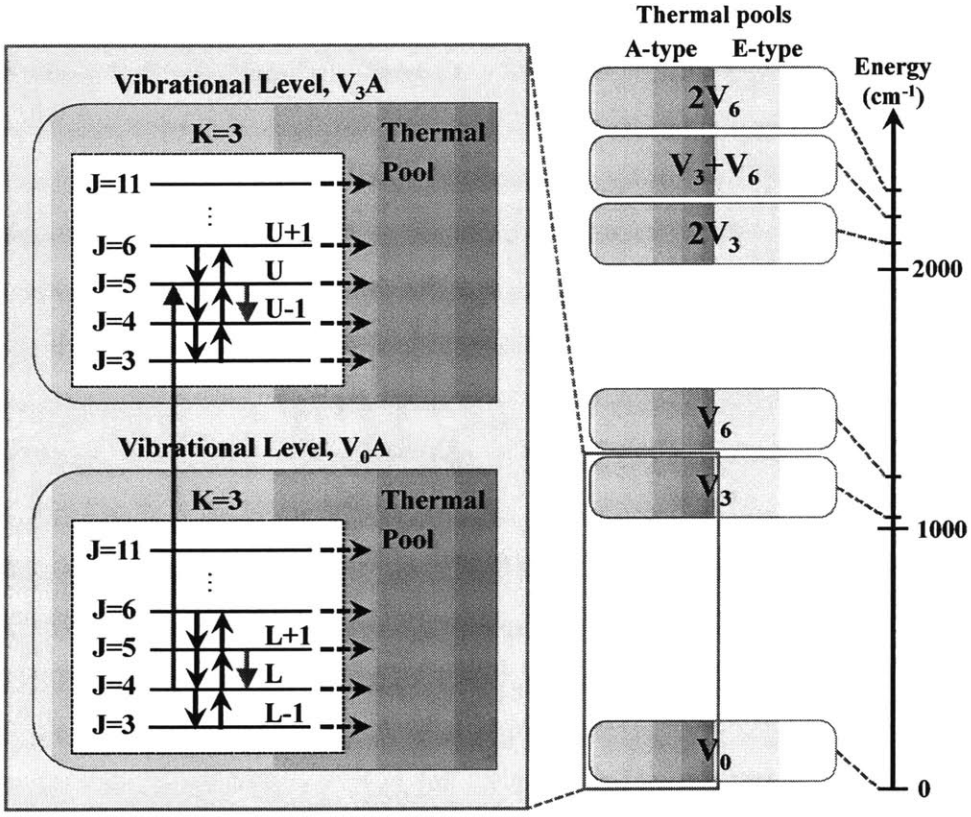

Figure 4-1: Illustration of vibrational energy levels of $^{13}CH_3F$ in a six-level model. A collection of rotational states under rotational equilibrium can be modeled as a thermal pool. Each vibrational level has two thermal pools with symmetry types of A and E. The six-level model considers the six lowest vibrational levels (12 thermal pools) and nine K=3 non-thermal states, each in V_0A and V_3A. J=4 in V_0A and J=5 in V_3A are directly connected by the pump (blue arrow), and are denoted as L and U, respectively. Their adjacent non-thermal states are denoted as L$\pm$1 and U$\pm$1, respectively, and population inversions (red arrows) are created between L+1 and L (refilling inversion) and U and U-1 (direct inversion). Details on each process are described in the text.

connected to the pump (as well as several neighboring states) no longer maintain rotational equilibrium with their respective thermal pools; they include additional population that cannot be described by Boltzmann statistics at thermal equilibrium. Thus, this cluster of rotational states can no longer be considered part of the thermal pools and must be modeled separately as "non-thermal" states, labeled as J=3, J=4, ... , J=11 in Fig. 4-1. As a result, the population of any of these rotational states can be expressed as the sum of its thermal and non-thermal parts, where the non-thermal part is the amount of population that differs from thermal equilibrium. The total population of a non-thermal rotational state at J=i is

$$N_{J=i}^{tot} = C_{J=i} \cdot N_{pool} + N_{J=i}\,, \tag{4.2}$$

where $C_{J=i}$ is the rotational state fraction of the corresponding thermal pool population N_{pool}, and $N_{J=i}$ is the excess or deficient non-thermal population induced by the pump and subsequent collisions. Note that $N_{J=i}$ is initially zero when the pump is off and is either positive or negative for only a few rotational states in V_3 or V_0, respectively, when the pump is on.

The six-level model in Fig. 4-1 assumes nine non-thermal states (J=3 to J=11) in V_0A and V_3A each, all with the same K=3 quantum number as the states connected by the pump (blue arrow in Fig. 4-1): J=4 in V_0A and J=5 in V_3A. These lower and upper non-thermal states are denoted as L and U, respectively, and their adjacent states are L$\pm$1 and U$\pm$1. Population inversions (red arrows in Fig. 4-1) are created between L+1 and L (refilling inversion) and U and U-1 (direct inversion). This six-level model is an extension of the one presented in Ref. [49] where low-pressure behavior was the main focus. The need to predict high-pressure behavior motivated the extension of the vibrational energy level system. In Section 4.7, another vibrational energy level system will be presented to predict even higher-pressure behavior. The important collisional processes and how their rates are handled will be discussed shortly, but first we need to discuss the pump process and how non-thermal populations are created since it is through the non-thermal states that the OPFIR rotational

population inversion occurs.

4.3 Pump Rate

The IR pump creates the rotational inversion, and the pump rate (R_{pump}) is defined as

$$R_{pump}(\mathbf{r},t) = p_{L\to U}(\boldsymbol{r},t)\cdot\Delta N_{pump}(\boldsymbol{r},t)\,, \tag{4.3}$$

where $p_{L\to U}(\boldsymbol{r},t)$ is pump transition rate that is directly proportional to the pump power P_{pump} [49], and $\Delta N_{pump}(\boldsymbol{r},t)$ is total molecular density difference between the two rotational states L (J=4, K=3 in V_0A) and U (J=5, K=3 in V_3A) connected by the pump. As defined in Section 4.2, total molecular density in a rotational state is the sum of the corresponding fraction of the thermal population and non-thermal population (if it has any).

In order to describe the pump rate accurately, the velocity distribution of the molecules must be considered. Molecules move in random directions at velocities distributed by the Maxwell-Boltzmann statistics, resulting in a velocity distribution with respect to a reference frame at rest. When a transition occurs, the Doppler effect broadens the width of the distribution of frequencies through

$$\frac{\nu-\nu_0}{\nu_0} = \frac{v}{c}\,, \tag{4.4}$$

where ν_0 is the IR transition frequency which corresponds to the energy difference between L and U. Fig. 4-2 shows a relative velocity (or frequency) distribution of the total (red), thermal (blue dashed), and non-thermal (blue solid) populations of L and U at steady state under $P = 300$ mTorr and $P_{pump} = 10$ W. Note that ν_0 is close to but typically not equal to the IR pump frequency ν_{pump}, and their difference $|\nu_{pump}-\nu_0|$ is referred to as the pump offset frequency ν_{offset}. Without loss of generality, we reference ν_0 to zero in Fig. 4-2; thus, the pump frequency is located at ν_{offset}.

When the pump is off, both L and U have inhomogeneously Doppler-broadened

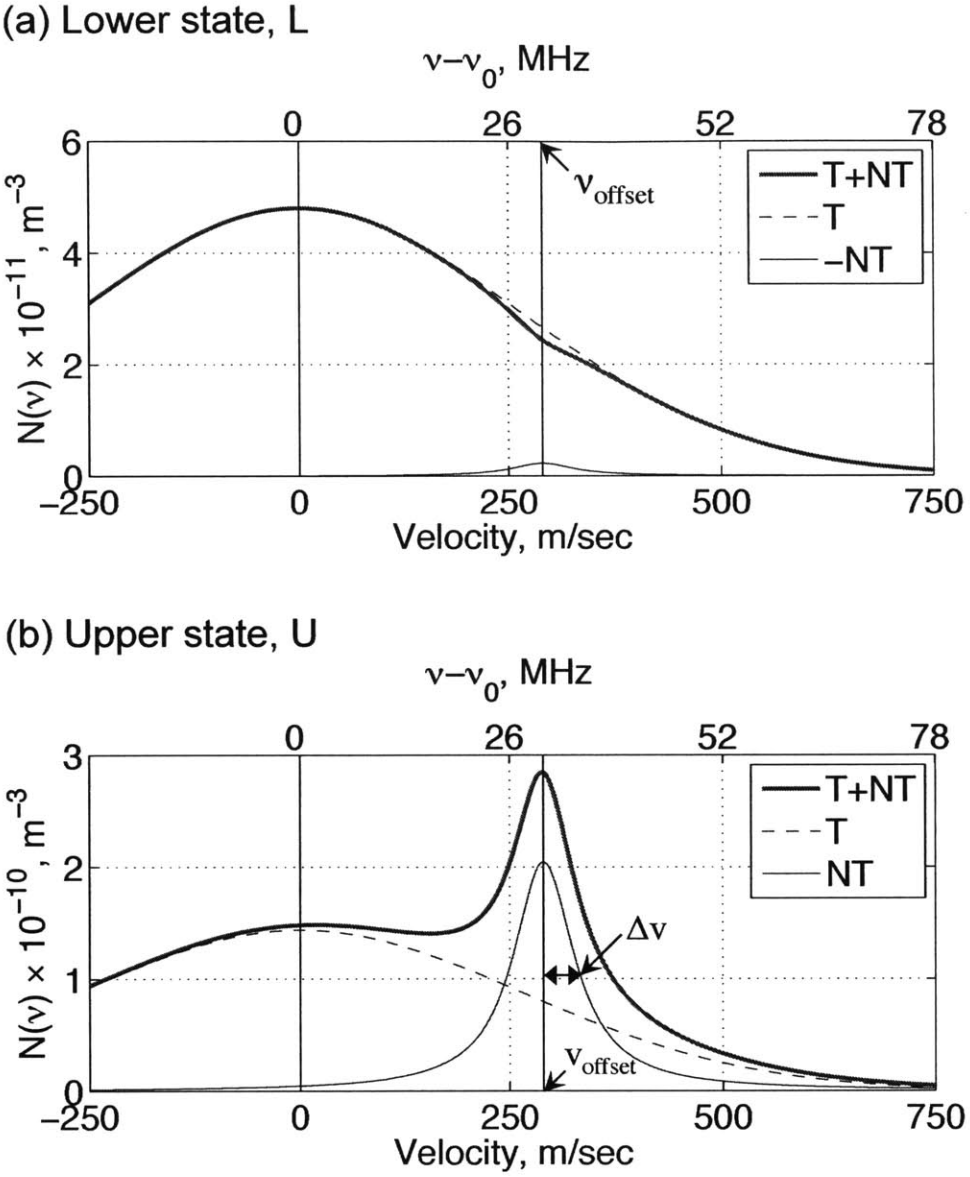

Figure 4-2: Velocity (or IR frequency) distribution of the steady-state molecular population for the L (J=4, K=3 in V_0) and U (J=5, K=3 in V_3) states at P = 300 mTorr induced by a 10 W pump. The total population (T+NT) is divided into the thermal (T) and the non-thermal (NT) parts. The homogeneously broadened ($\pm\Delta\nu_P$) Lorentzian non-thermal velocity subclass pumped by the laser is offset by ν_{offset} = 30 MHz from the center of inhomogeneously broadened ($\pm\Delta\nu_D$) Gaussian thermal background. Thus, the pump action creates a Lorentzian dip(peak) centered at ν_{offset} on the Gaussian profile of L(U). v_{offset} and Δv are equivalent to ν_{offset} and $\Delta\nu_P$, respectively, in velocity.

Gaussian frequency distributions of width ($\pm\Delta\nu_D$) centered at zero (which represents ν_0) with populations derived from their respective thermal pool. The pump action changes the frequency distribution of the total molecular density of L and U. When the pump is turned on, the molecules in the homogeneously pressure-broadened Lorentzian velocity subclass of width ($\pm\Delta\nu_P$) centered at ν_{offset} (which represents ν_{pump}) are transferred from L to U. Thus, a non-thermal Lorentzian dip(peak) centered at ν_{offset} appears on the thermal Gaussian profile of L(U). Note that in Fig. 4-2 the relative contribution of the non-thermal part (blue solid) to the total molecular population (red) in V_3 is more significant than that in V_0 due to the smaller thermal pool population in V_3.

$\Delta N_{pump}(\boldsymbol{r}, t)$ is calculated by integrating the difference between the two total molecular population profiles (red solid lines in Fig. 4-2) within the velocity subclass ($\pm\Delta\nu_P$) centered at ν_{offset} after degeneracy ($g_{J=j} = 2j + 1$) is removed. At a given radial distance $\boldsymbol{r}$ and time t, ΔN_{pump} is defined as:

$$\Delta N_{pump} = \int_{\nu_{offset}-\Delta\nu_P}^{\nu_{offset}+\Delta\nu_P} \Delta N_{pump}(\nu)\,\mathrm{d}\nu\,, \tag{4.5}$$

$$\Delta N_{pump}(\nu) = \frac{C_{\mathrm{L}} \cdot N_{pool}^{\mathrm{V_0A}} \cdot f_D(\nu) + N_{\mathrm{L}}^{\mathrm{V_0A}} \cdot f_P(\nu, \nu_{offset})}{g_{\mathrm{L}}} - \frac{C_{\mathrm{U}} \cdot N_{pool}^{\mathrm{V_3A}} \cdot f_D(\nu) + N_{\mathrm{U}}^{\mathrm{V_3A}} \cdot f_P(\nu, \nu_{offset})}{g_{\mathrm{U}}}. \tag{4.6}$$

$N_{pool}^{\mathrm{V_{0(3)}A}}$ and $N_{\mathrm{L(U)}}^{\mathrm{V_{0(3)}A}}$ are thermal pool and non-thermal population, respectively, as defined in Section 4.2. $f_D(\nu)$ and $f_P(\nu, \nu_{offset})$ are area-normalized Doppler-broadened Gaussian and pressure-broadened Lorentzian functions, respectively,

$$f_D(\nu) = \frac{1}{\Delta\nu_D}\sqrt{\frac{\ln 2}{\pi}} \exp\left[-\ln 2 \cdot \left(\frac{\nu}{\Delta\nu_D}\right)^2\right] \tag{4.7}$$

$$f_P(\nu, \nu_{offset}) = \frac{1}{\pi}\left[\frac{\Delta\nu_P}{(\nu - \nu_{offset})^2 + (\Delta\nu_P)^2}\right], \tag{4.8}$$

for which the half-width at half-maximum values of $f_D(\nu)$ and $f_P(\nu, \nu_{offset})$ for $^{13}CH_3F$ are defined as:

$$\Delta\nu_D = \frac{\nu_0}{c}\sqrt{-\ln 2 \cdot \frac{2k_BT}{m}} = 3.58 \times 10^{-7}\nu_o\sqrt{\frac{T}{m}} \tag{4.9}$$

$$\Delta\nu_P = \frac{1}{2\pi\Delta\tau} \approx 15(\text{MHz/Torr}), \tag{4.10}$$

where m is molecular mass in AMU and $\Delta\tau$ is mean collision time [60].

Within the velocity subclass centered at ν_{offset}, the upper state population increases and the lower state population decreases, and the difference in population is reduced as the pump operates. Since the pump power absorption is proportional to this difference in population $\Delta N_{pump}(\boldsymbol{r}, t)$, when the difference approaches zero, pump saturation occurs. Pump saturation is strongly evident in very low-pressure regime (< 20 mTorr for our 0.25 cm radius cell) because the number of molecules is small and the velocity subclass is narrow. When this happens, power-broadening increases the width of the non-thermal feature, somewhat mitigating pump saturation and maintaining $R_{pump} > 0$. These frequency- and pump power-dependent thermal and non-thermal populations are also important at higher pressure, as their relative strength determines the population inversion, as will be discussed in detail in Section 4.6.

In addition, the pressure-dependent absorption of the IR pump beam must be considered for more accurate lasing predictions. The pump power P_{pump} decreases exponentially as the pump beam propagates through the cavity through Beer's law ($e^{-\alpha_{IR}L}$), where α_{IR} is the IR absorption coefficient of the laser gas at the pump frequency ν_{pump} [60] and L is the distance. Clearly the pump is most effective at the entrance of the cavity and least effective at the rear. Therefore, the effective pump power in the cell, $P_{pump}^{eff} = P_{pump} \cdot \kappa$, may be used, where P_{pump} is the incident pump power and $\kappa = \left(\int_0^{L_{cell}} \mathrm{e}^{-\alpha_{IR}L}\,\mathrm{d}L\right)/L_{cell} = (1 - \alpha_{IR}L_{cell})/\alpha_{IR}L_{cell}$ as defined in Ref. [49]. As shown in Fig. 4-3, for a given pump power, α_{IR} increases with pressure, so κ decreases with pressure. For a given pressure, α_{IR} and κ also depend on pump

power because of the population redistribution induced by the pump. Specifically, α_{IR} decreases with increasing pump power as a result of pump saturation: a higher pump power leads to faster saturation of the pumped transition velocity subclass, reducing absorption and increasing κ.

α_{IR} also determines the optimal cavity length for a given pressure and pump power. The pump power will be highly absorbed in the front section of the cavity, so the strongest lasing action will occur there. However, if the cell is too long, the back of the cavity will not be pumped, and these un-pumped molecules will absorb the lasing field generated in the front of the cell, adding unnecessary loss to the system. To avoid this, the cavity length should satisfy $2 \times L_{cell} < 1/\alpha_{IR}$. The factor of two arises from the round trip distance of the pump beam, which results in a stricter upper bound of L_{cell}. Fig. 4-3(b) plots $1/\alpha_{IR}$ and $2 \times L_{cell}$. The cell length used in our experiment is shorter than $1/2\alpha_{IR}$ throughout the range of operating pressure considered in this work, so there is minimal loss generated from any un-pumped molecules.

4.4 Wall Collision Rate

The primary vibrational relaxation pathways of molecules are collisions with the cell wall and through extremely rare hard inter-molecular collisions. A thorough treatment of the diffusive process by which wall collisions occur is presented next, and the plethora of molecular collision processes will be addressed in Section 4.6.

The wall collision process in a cylindrical cell is dependent on molecular diffusion, which acts to produce a radial spatial variation in the molecular populations. Furthermore, molecular collisions with the wall produce a Boltzmann distribution of rotational and vibrational population based on the wall temperature (assumed to be 300K in this work). Therefore, the majority of vibrationally excited molecules are de-excited to V_0 after wall collision and are distributed thermally in the two thermal pools (A and E) while preserving symmetry type. Wall collisions in Ref. [49] were modeled by defining balanced excitation and de-excitation level-to-level rate constants among the excited thermal pools and V_0. Their model approximated the

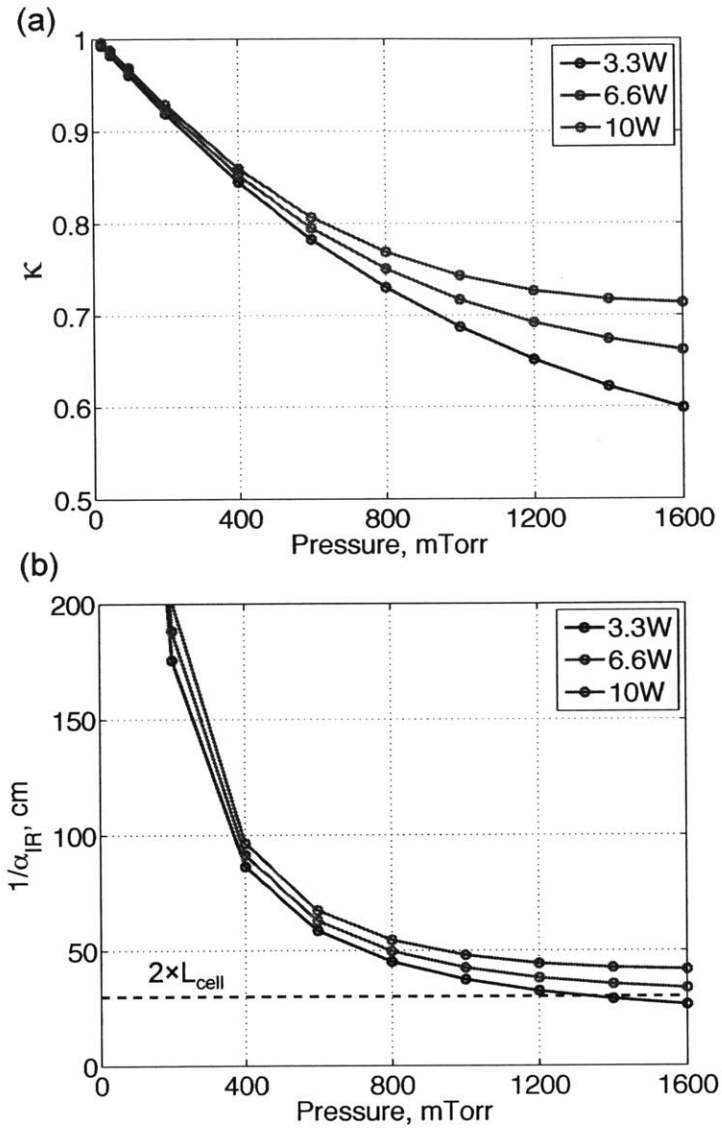

Figure 4-3: (a) κ as a function of pressure and pump power. (b) α_{IR}^{-1} as a function of pressure and pump power. This represents the upper bound of optimal cell length, above which un-pumped molecules will cause additional absorption loss. The dotted line corresponds to $2 \times L_{cell}$.

wall collision rate at a radial position x (where $0 < x < R$) as $k_w = v\lambda/(R-x)^2$ if $x \in [0, \max(0, R-\lambda)]$ and $k_w = v_{abs}/(R-x)$ if $x \in [\max(0, R-\lambda), R]$. Here, λ is the pressure-dependent mean free path, v is the average relative velocity between molecules, and v_{abs} is the average absolute velocity of molecules. Even though k_w is qualitatively correct in that it increases in value as x approaches the wall, this simplified treatment of the wall collision rate was increasingly inadequate at high operating pressures (> 1 Torr).

We rigorously re-derived wall collision rate k_w from first principles by considering the geometry of the laser cavity and simple molecular dynamics. k_w represents the fraction of molecules that will collide with the cavity wall per unit time when starting from a given radial position in the cell. We considered first order velocity-randomizing gas kinetic collisions. At a given temperature T and pressure P, the mean free path λ is defined as $\lambda = 0.732\,T/P\,\sigma_{GK}$, where σ_{GK} is gas kinetic collision cross section. Here, λ is in cm, P is in mTorr, and σ_{GK} is in $\mathring{A}^2$. It may be assumed, without loss of generality, that only molecules located within λ of the wall have a chance to collide with it and be de-excited. Therefore, the fraction of those molecules that reach the wall may be estimated as the fractional surface of a sphere with radius λ that intersects the cylindrical cell wall.

As illustrated in Fig. 4-4(a), the fraction of molecules that collide with the wall $f_w(x)$ at a given radial position x is equal to the fractional surface of the sphere intercepting the cylinder and is given by

$$f_w(x) = \frac{2 \cdot \int_{\theta_0}^{\pi/2} 2\lambda^2 \sin\theta \cos^{-1}\left(\frac{R^2-\lambda^2\sin^2\theta-x^2}{2\lambda x \sin\theta}\right) \mathrm{d}\theta}{4\pi\lambda^2}, \tag{4.11}$$

where $\theta_0 = \sin^{-1}((R-x)/\lambda)$ (see Ref. [61]). $f_w(x)$ is zero for $x \in [0, R-\lambda]$, and gradually increases to a number slightly larger than 0.5 at $x = R$. For clarity, Fig. 4-4(a) shows a horizontal cross section of the system at $\theta = \pi/2$, where θ is the polar angle measured from the vertical axis of the sphere. $\psi(\theta)$ measures the angle at which the horizontal cross section of the sphere intercepts the cylinder at θ. For a molecule that can reach the cavity wall, its actual distance to the wall varies with its starting

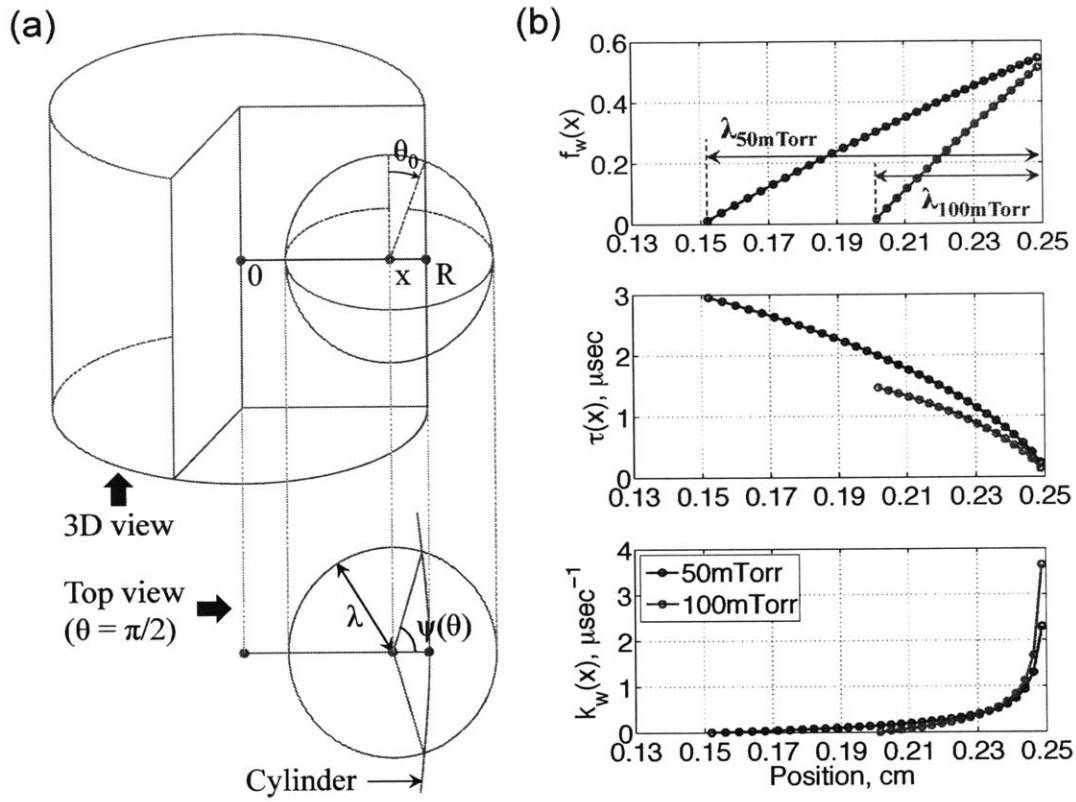

Figure 4-4: (a) Schematic diagram for wall collision rate derivation. When a molecule is located at x, $f_w(x)$ is the fraction of molecules that can collide with the cell wall, which is equal to the surface fraction of the sphere with radius λ lying outside the cylinder. $\tau(x)$ is the average time to reach the wall from x. Then, $k_w(x)$ is simply $f_w(x)/\tau(x)$. (b) $f_w(x)$, $\tau(x)$ and $k_w(x)$ at 50 and 100 mTorr are plotted.

position and direction of motion. By averaging over all directions $\psi(\theta)$ towards the wall, the average distance to the wall at a given radial position x becomes

$$\bar{l}(x) = \frac{\int_{\theta_0}^{\frac{\pi}{2}} \int_0^{\psi(\theta)} l(x,\theta,\psi') \cdot \sin\theta \, \mathrm{d}\psi' \, \mathrm{d}\theta}{\int_{\theta_0}^{\frac{\pi}{2}} \int_0^{\psi(\theta)} \sin\theta \, \mathrm{d}\psi' \, \mathrm{d}\theta}, \tag{4.12}$$

where

$$l(x,\theta,\psi') = \sqrt{\left(\frac{R-x}{\tan\theta}\right)^2 + \left(-x\cos\psi' + \sqrt{x^2\cos^2\psi' - x^2 + R^2}\right)^2}. \tag{4.13}$$

The denominator is the solid angle, and $\psi(\theta) = \cos^{-1}\left(\frac{R^2-\lambda^2\sin^2\theta-x^2}{2\lambda x\sin\theta}\right)$ [61]. Note that the average distance to the wall is only a function of radial position x, but the time to reach the wall varies with the molecule's speed. Since a molecule's speed follows a Maxwell-Boltzmann distribution, the average time $\tau(x)$ for the molecule at x to reach the wall is expressed as

$$\tau(x) = \int_0^\infty \frac{\bar{l}(x)}{v} \cdot f_{MB}(v) \, \mathrm{d}v, \tag{4.14}$$

where $f_{MB}(v) = \sqrt{\left(\frac{m}{2\pi k_B T}\right)^3} \cdot 4\pi v^2 \cdot \exp\left[-\frac{mv^2}{2k_B T}\right]$. Then, the wall collision rate is simply

$$k_w(x) = \frac{f_w(x)}{\tau(x)}. \tag{4.15}$$

Fig. 4-4(b) plots $f_w(x)$, $k_w(x)$, and $\tau(x)$ at 50 and 100 mTorr. $k_w(x)$ is zero within $x \in [0, R-\lambda]$ and rapidly increases beyond $R-\lambda$. Note that the non-zero $k_w(x)$ range narrows as pressure increases.

In Fig. 4-5, examples of time-resolved THz double resonance spectra for representative V_3A, V_3E, V_6A, and V_6E rotational transitions in a radius R = 1 cm cell are presented [55]. Double resonance data reveal the propensities and rates of collisional processes moving molecules into and out of the monitored levels, from which the related rate constants may be extracted. Ref. [55] experimentally obtained the

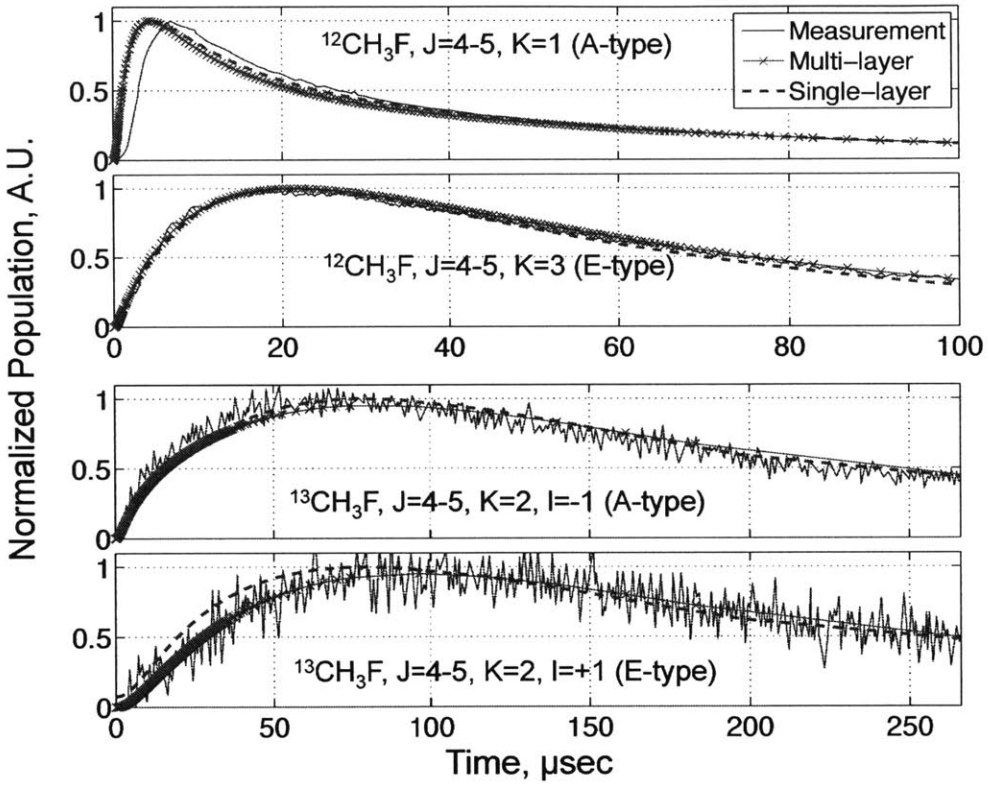

Figure 4-5: Double resonance experiment for V_3A and V_3E at 20mTorr (top two plots) and for V_6A and V_6E at 40mTorr (bottom two plots). A 0.5 μsec pulse pump of 1W was used for both experimental measurement and simulation. The experiment data (blue) was obtained from Everitt *et al.* (1993). The simulation data were obtained using multi-layer system (green) and single-layer system (red) (see text for details on the definitions of these two systems).

double resonance data by pumping the cavity with a short laser pulse (0.5 μsec, 1 W) and measuring the flow of population into and out of the various levels or thermal pools. The top two plots show the time-varying absorption of representative transitions in the V_3A and V_3E thermal pools of $^{12}CH_3F$ at 20 mTorr, while the bottom two plots show the evolving absorption of V_6A and V_6E of $^{13}CH_3F$ at 40 mTorr. Then, the temporal behavior of the model (using gas kinetic collision cross section $\sigma_{GK} = 44.1\text{Å}^2$ [62]) is compared to the experimentally measured double resonance data using the rate constants in Table 4.1 and without any fitting parameters. From Fig. 4-1, the pump (blue arrow) excites molecules from V_0A to V_3A. The excited molecules then transfer to other thermal pools such as V_3E and V_6 through various collision processes (e.g. V-swap [52, 55, 56]), and are eventually Boltzmann distributed through wall collisions. This explains why the time to reach the peak is shortest for V_3A in Fig. 4-5 (since the pump excites molecules directly to V_3A) and other thermal pools reach their peaks later. Since wall collisions play a large role in the temporal evolution, excellent agreement between the experimental data and the model predictions confirm the adequacy of the wall collision rate developed here [1].

Interestingly, the double resonance behavior predicted from the multi-layer model can be obtained from a rather simple single-layer model too (red dashed lines in Fig. 4-5), if the radial distribution of population need not be modeled [55]. In the multi-layer model, the cavity is divided into multiple (50 in this work) concentric cylindrical layers to account for the spatial variation and diffusion of the molecules. The wall collision rate of each layer is calculated at the middle of the layer. On the contrary, the single-layer model has only one layer. Thus, a different wall collision rate definition must be used. Assuming that gas molecules are scattered uniformly throughout the cell, the average distance traveled between collisions is the mean free path λ. Since velocity is randomized after collision, the wall collision rate can be calculated as $k_w = 0.31/P \cdot R^2$ (μsec^{-1}) for CH_3F at 300K [60], where P is pressure

[1] Disagreement at early time in the top plot is due to an overlapping non-thermal transition of $^{12}CH_3F$. In $^{12}CH_3F$, the pump transition occurs from J=12, K=2 state, but its small overlap with J=12, K=1 state pumps both states at early time. For this reason, a lag in the peak is observed from the experiment.

in mTorr and R is cavity radius in cm. It is worth noting that the single-layer model saves computation time due to its simplicity, but the multi-layer model simulates more realistic diffusion and population excitation gradients and can be easily expanded to represent spatially non-uniform systems. Indeed, the multi-layer model is necessary to determine the spatial distribution of inversion and its overlap with cavity modes required to predict OPFIR laser performance [49].

4.5 Experimental measurements

Experimental THz laser output was newly measured in this study. A heterodyne receiver system was used to measure the pressure- and power-dependent performance of the direct (U $\rightarrow$ U-1) and refilling (L+1 $\rightarrow$ L) inversions in a compact OPFIR laser. The OPFIR laser consisted of a copper cylindrical laser cavity with $R = 0.25$ cm and $L_{cell} = 15$ cm [50]. The front and the rear reflectors were gold (Au) coated with a 1 mm diameter pinhole in the center of the front reflector that serves as the input port for the IR pump radiation and as the output coupler for the molecular laser. The OPFIR laser was pumped by a grating tuned continuous wave CO_2 laser operating on the 9P(32) laser line at 9.657 μm. The output power of the OPFIR was measured by a Virginia Diodes, Inc. heterodyne receiver with a local oscillator (LO) operating at 247.0008 GHz so that the direct inversion at 245.3508 GHz and the refilling inversion at 248.5594 GHz produce an intermediate frequency (IF) of 1650 and 1559 MHz, respectively. The IF output was monitored with an Agilent N9322C spectrum analyzer with integrated power reported over a 100 MHz bandwidth centered on the laser transition under examination.

Measurements were performed on an isotopically purified sample of $^{13}CH_3F$. The laser mode producing the highest output gain for a specific inversion was assumed to be the mode that maintained lasing at the highest operating pressure. Therefore, either the direct or refilling lasing transition was initially measured at an intermediate $^{13}CH_3F$ pressure that produced strong emission, and the cavity length was adjusted to maximize the laser power. Next, the pressure was increased, and slight cavity length

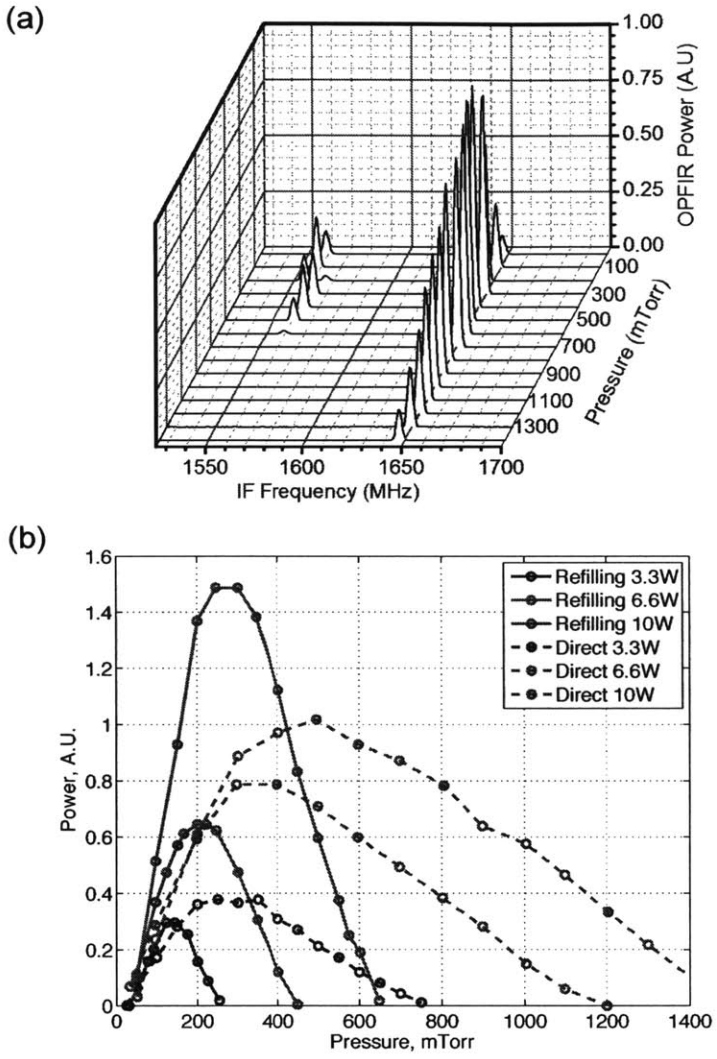

Figure 4-6: (a) Experimentally measured THz laser output power as a function of pressure and pump power for the direct (right) and refilling (left) inversions in $^{13}CH_3F$, plotted as a function of the intermediate frequency (IF) produced when the laser radiation was mixed with a local oscillator operating at 247.0008 GHz. (b) Plot of the measured relative laser power as a function of pressure and incident pump power for both inversions. Lasing was observed for the direct inversion at pressures as high as 1.7 Torr. (Note: the direct inversion peaks appear stronger than the refilling inversion peaks in (a). The data was obtained when the system was tuned to maximize the direct inversion strength.)

adjustments were made, until a pressure was reached at which the lasing action was quenched. After reducing the pressure slightly to re-establish lasing, the OPFIR laser power was recorded as the pressure was systematically lowered by cryogenic trapping to produce the curves in Fig. 4-6. The pressure lowering and measurement were repeated until no lasing was observed for one inversion, then the measurements were repeated for the strongest mode associated with the other inversion. The process was performed for pump powers of 3.3, 6.6, and 10 W coupled into the laser cavity.

Because the existing models cannot reproduce this data, several characteristics should be recognized that must be demonstrated by any successful model of OPFIR laser performance. First, notice that the laser operated at pressures much higher than the model-predicted cutoff pressure of 0.44 Torr in Ref. [50]. The direct inversion was observed to operate up to 1.7 Torr for 10 W of pump power. Second, the cutoff pressure for the direct inversion increased linearly with pump power, while existing models predicted a cutoff pressure that was independent of pump power [50]. Third, notice that the THz power decreased linearly with increasing pressure at a constant slope that did not change with pump power (i.e. the lines are parallel). This indicates that a maximum cutoff pressure was not being approached and that even higher operating pressures could have been achieved with more pump power. Fourth, the pressure at which maximum THz power was produced increased with increasing pump power for both inversions. Fifth, the refilling inversion grows faster in strength with increasing pump power than does the direct inversion, and it actually produced the most THz power for the strongest pump power. Finally, the refilling inversion quenches at a much lower pressure in a manner that increases linearly with pump power, just as the direct inversion did, indicating that even more THz power and higher pressure operation can be achieved for the refilling transition with more pump power.

4.6 Low-pressure regime

4.6.1 Rate equation modeling

Following the action of the pump to move ground state molecules from L (J=4, K=3 in V_0A) to U (J=5, K=3 in V_3A), laser action is achieved by the creation of population inversion (upper red arrow in Fig. 4-1) between U and the rotational state U-1 immediately below it (J=4, K=3 in V_3A). This direct population inversion (ΔN^d_{inv}) is the total molecular density difference between these two rotational states per degenerate state, accounting for both the non-thermal population and corresponding fraction of the thermal population as

$$\Delta N^d_{inv} = \frac{C_{\mathrm{U}} \cdot N^{\mathrm{V_3A}}_{pool} \cdot f_{SHB} + N^{\mathrm{V_3A}}_{\mathrm{U}}}{g_{\mathrm{U}}} - \frac{C_{\mathrm{U-1}} \cdot N^{\mathrm{V_3A}}_{pool} \cdot f_{SHB} + N^{\mathrm{V_3A}}_{\mathrm{U-1}}}{g_{\mathrm{U-1}}}. \tag{4.16}$$

Here, f_{SHB} (spectral hole burning) accounts for the fraction of thermal molecules in the pumped velocity subclass within Δv centered at v_{offset} (Fig. 4-2), and is approximated as $f_{SHB} = \int_{v_{offset}-\Delta v}^{v_{offset}+\Delta v} f_D(v)\,\mathrm{d}v$.[2] From Eq. (4.16), the direct population inversion exists as long as the population density difference between the non-thermal populations of U and U-1 is greater than the difference in their respective portions of the thermal pool over the width of the SHB centered at v_{offset}.

To appreciate the significance of this, consider the refilling inversion ΔN^r_{inv} (lower red arrow in Fig. 4-1) between L and L+1 (J=5, K=3 in V_0A), which may be calculated as an obvious modification of Eq. (4.16). Because the thermal populations in L and L+1 are so large, it would be nearly impossible for the pump to deplete L enough for the non-thermal population to overcome it and create an inversion. However, the non-thermal population needs only to overcome the thermal population in the pumped velocity subclass to produce lasing. Therefore, correct prediction of

[2]Better approximation of f_{SHB} can be achieved by considering the velocity distribution of molecules for the THz transition separately and integrating that over a proper velocity range. This requires further research, and will be presented in: Jeongwon Lee, Dane J. Phillips, Samuel G. Holliday, Song-Liang Chua, Jorge Bravo-Abad, Marin Soljacic, and Henry O. Everitt, "Terahertz lasing action in high-pressure optically-pumped molecular gases" (in preparation).

the refilling transition depends sensitively on how accurately f_{SHB} is calculated. The same methodology is then applied to the direct transition, for which inversion is much easier to achieve over the small thermal populations in V_3 at low pressures. However, achieving a direct inversion grows much more challenging at high pressures as the vibrational bottleneck dramatically increases the quenching thermal populations and pressure broadening increases the width of the SHB. The remaining discussion will be focused primarily on this high pressure behavior of the V_3 direct inversion, but the V_0 refilling inversion can also be understood in a very similar way.

Prior models such as those presented in Ref. [44, 45, 49, 53, 63] included at most three lowest vibrational levels: V_0, V_3 and V_6. Pump-induced population inversion is responsible for lasing action, but becomes quenched when the thermal contribution exceeds the non-thermal contribution in the states involved. Thus, the thermal pool population plays an important role in determining whether or not lasing can occur. As pressure increases, the population in the thermal pools of excited vibrational levels (e.g. V_3) increases as diffusion toward the walls slows; this reduces the molecular collisions with wall and hence, their de-excitation back to the ground state. This vibrational bottleneck is the principal mechanism by which lasing is quenched, but is incorrectly predicted from the prior models due to the small number of vibrational levels. Consequently, thermal pool population is overestimated and lasing is underestimated. Since numerous vibrational state-changing collisional processes become increasingly effective as V_3 fills, adding more high-lying vibrational levels and these additional energy transfer processes allows the excited molecules to be distributed among vibrational levels above V_3 [50]. However, because of the large number of vibrational levels involved and the unknown collisional rate constants connecting them, no satisfactory method for simulating these phenomena has yet been developed. The main goal of this work is to report a methodology to model this effectively.

To understand the new approach described here, first consider only two vibrational levels, V_0 and V_3. In the high-pressure regime, V_3 fills up much faster than it should because there are no other vibrational relaxation channels through which molecules in V_3 may be transferred out. The artificially expanded population in V_3

Table 4.1: Model parameters

Parameters	(in $Å^2$)
Gas kinetic collision cross section, σ_{GK}	44.1 (Ref. [62])
Dipole-Dipole cross section, σ_{DD}	320 (Ref. [51])
SPT cross section, σ_{SPT}	137 (Ref. [52,56])
$V_3 \rightarrow V_6$ cross section, σ_{36}	3.21/2 = 1.61 (Ref. [55,65])
V-swap cross section, σ_{VS}	21.0 (Ref. [52,56])
V-split cross section, σ_{VSp}	12.4 (Ref. [65])
Mass, m (AMU)	35
IR transition frequency, ν_0 (THz)	31.042748
Pump offset frequency, ν_{offset} (MHz)	30
THz transition frequency (Direct/Refilling), ν_{THz} (GHz)	245.38/248.56

is increasingly trapped there, prematurely triggering the vibrational bottleneck and quenching the inversion created by the pump. Indeed, it can be shown that this mechanism produces a maximum lasing pressure regardless of pump intensity [50]. By adding more vibrational levels and the processes that connect them to V_3, a more realistic model can be produced.

As a first attempt to simulate the effect of additional vibrational levels, a six-level multi-layer model was constructed in which each vibrational level contains two symmetry-defined thermal pools and all the associated collisional rate constants are known (see Table 4.1). In Table 4.1, the factor of two in σ_{36} was introduced to take account of double degeneracy in V_6. In addition, a total of 18 rotational states, nine each in V_0A and V_3A, contain non-thermal population (see Fig. 4-1). The fastest molecular collisional mechanism [51,57] connecting the rotational states, which is only observable among states with non-thermal population, is the long-range dipole-dipole collision for which the selection rule is $\Delta J = \pm 1, \Delta K = 0$ [64] and the cross section is 320 $Å^2$ [51]. This mechanism is represented as vertical black arrows in Fig. 4-1. Detailed balance takes into account degeneracy and energy difference between two adjacent rotational states so that the system maintains or is driven toward steady state.

Other rotational state-changing collisions must also be modeled [64]. A class of collisional processes that have the effect of moving molecules among rotational states

of the same symmetry type has been observed [52, 56, 64]. The cumulative effect of these "symmetry preserving thermalization" (SPT) processes transfers molecules in all non-thermal states to the corresponding thermal pool of the same symmetry type. For symmetric top molecules with three-fold symmetry, this process requires the selection rule $\Delta K = 3n$, where n is an integer, and has been referred to as the K-swap process [49,51,52,55–59]. This process is represented as horizontal black dashed arrows in Fig. 4-1. The SPT process does not have reverse process from the thermal pool to the non-thermal states since the only mechanism that can create non-thermal states is the pump. Consequently, the non-thermal states are depleted by the SPT mechanism and return to zero when pump is turned off. The cross section for this process has been measured to be 137 $Å^2$ [52, 56].

Among thermal pools, molecules are transferred via a variety of non-resonant and near-resonant vibrational energy transfer processes [55, 56, 65]. Of the non-resonant type, the most common is the collisional process that transfers molecules between V_3 and V_6. The energy separation between those levels is $\sim$150 cm^{-1}, so collisions of V_3 or V_6 molecules with V_0 molecules can sometimes be hard enough to transfer a sufficient fraction of the 200 cm^{-1} translational energy to induce this vibrational transition. The cross section for this process has been measured to be 3.21 $Å^2$ [55,65].

Near-resonant vibrational energy transfer occurs when two colliding molecules exchange quanta of vibrational energy. The most common form of this collision occurs between a V_3 and a V_0 molecule, and the resonant energy exchange places the V_0 molecule in V_3 and vice versa while preserving the symmetry type of each. Because of the resonant nature of this exchange, the cross section is much larger, 21.0 $Å^2$ for CH_3F [52, 56]. Variants of this "V-swap" process abound, including the "V-split" process in which a molecule in $2V_3$ collides with a V_0 molecule producing two molecules in V_3, or the converse process in which two V_3 molecules collide to produce one V_0 and one $2V_3$ molecule. The cross section for V-split processes can also be large, the latter of which was measured to be 12.4 $Å^2$ [65]. The list of near-resonant collision processes is shown in Table 4.2, and the associated collisional cross sections are shown in Table 4.1. Most importantly, these V-split processes move molecules

Table 4.2: Near-resonant vibrational energy transfer collision processes (V_{36} = V_3+V_6)

A-symmetry	E-symmetry
$V_0A+V_3E \leftrightarrow V_3A + V_0E$	
$V_0A+V_6E \leftrightarrow V_6A + V_0E$	
$V_0A+2V_3A \leftrightarrow V_3A + V_3A$	$V_0E+2V_3E \leftrightarrow V_3E + V_3E$
$V_0A+2V_6A \leftrightarrow V_6A + V_6A$	$V_0E+2V_6E \leftrightarrow V_6E + V_6E$
$V_0A+V_{36}A \leftrightarrow V_3A + V_6A$	$V_0E+V_{36}E \leftrightarrow V_3E + V_6E$
$V_0A+V_{36}E \leftrightarrow V_3A + V_6E$ or $V_3E + V_6A$	
$V_0E+V_{36}A \leftrightarrow V_3A + V_6E$ or $V_3E + V_6A$	
$V_3A+V_3E \leftrightarrow V_0A + V_{23}E$ or $V_0E + V_{23}A$	
$V_6A+V_6E \leftrightarrow V_0A + V_{26}E$ or $V_0E + V_{26}A$	

from V_3 to higher lying vibrational levels, and they grow more effective as V_3 fills through the vibrational bottleneck.

These processes are important in that they are the only, albeit indirect, path that connects and equilibrates thermal pools of opposite symmetry types. The V-swap process also operates on non-thermal molecules, and thermalizes them by transferring them to the same symmetry type thermal pool in the other vibrational level. For example, when a non-thermal molecule in V_3A collides with a molecule in V_0E[A], they become thermal molecules in V_0A and V_3E[A], respectively. Thus, one non-thermal molecule in V_3A is effectively thermalized to V_3A and V_3E with equal probability. (This also applies to non-thermal molecules in V_0A.)

The rate equation for the rotational state U can be written as:

$$\begin{aligned}\frac{\mathrm{d}N_{\mathrm{U}}^{\mathrm{V_3A}}(\mathbf{r},t)}{\mathrm{d}t} = R_{pump} + \sum_{u=U\pm1}\left(DD_{in}^{u\to U} - DD_{out}^{U\to u}\right) \\ - SPT - VS + Diff\,,\end{aligned} \tag{4.17}$$

where R_{pump} is the pump rate from Eq. (4.3), $DD^{i\to j} = k_{DD}^{i\to j}\cdot N_{\mathrm{U}}^{\mathrm{V_3A}}(\mathbf{r},t)$ is the dipole-dipole collision rate, $SPT = k_{SPT}\cdot N_{\mathrm{U}}^{\mathrm{V_3A}}(\mathbf{r},t)$ is the SPT process rate, $VS = k_{VS}\cdot N_{\mathrm{U}}^{\mathrm{V_3A}}(\mathbf{r},t)$ is the non-thermal V-swap process rate, and $Diff = D\cdot\nabla_{\mathbf{r}}^2 N_{\mathrm{U}}^{\mathrm{V_3A}}(\mathbf{r},t)$ is the spatial diffusion rate, where D is the diffusion constant [49]. The rate constants

can be derived from the corresponding cross sections: $k_i = n_{tot} \cdot v\, \sigma_i = \left(\frac{P}{RT}\right) \cdot \sqrt{\frac{16kT}{\pi m}}\, \sigma_i$, where n_{tot} is the total molecular density.

As shown in Fig. 4-1, molecules are pumped from L to U, and through dipole-dipole collisions they rapidly transfer into adjacent rotational states (e.g. U+1 and U-1) with the same K quantum number. These non-thermally distributed pumped molecules may also transfer into V_3 thermal pools through SPT (same symmetry) process or V-swap (both symmetry types). Since SPT preserves symmetry type, only V_0A and V_3A can receive molecules from the non-thermal states created by the pump, while the V-swap process move molecules into thermal pools and vibrational levels of both symmetry types. Spatially, the molecules also move diffusively between adjacent layers through random walk - velocity scrambling gas kinetic collisions - until the system reaches steady state. For rotational states other than U or L, the rate equations have the same form as Eq. (4.17), except the pump rate term.

The number of the non-thermal states that must be modeled depends on the relative cross sections for the dipole-dipole mechanisms, and the SPT and V-swap mechanisms. The former redistributes molecules among the non-thermal rotational levels, while the latter two mechanisms depopulate these levels. Since the probability of a $\Delta J = +1$ collision is generally similar to the probability of a $\Delta J = -1$ collision, the dipole-dipole process distributes non-thermal populations in a random walk manner. Consequently, it is difficult for a non-thermal molecule to reach rotational states more than $[(\sigma_{SPT} + \sigma_{VS})/(\sigma_{DD} + \sigma_{SPT} + \sigma_{VS})]^{-1}$ away from L or U. This number is rounded up to ± 4 for $^{13}CH_3F$, which is why nine of these states were modeled in each of V_0 and V_3 here.

The rate equation for the representative thermal pool V_3A can be written as:

$$\begin{aligned} \frac{\mathrm{d}N_{pool}^{\mathrm{V_3A}}(\mathbf{r},t)}{\mathrm{d}t} &= \sum_u VV^u - Wall + RD \\ &\quad + \sum_i \left(SPT^i + VS^i\right) + Diff\,, \end{aligned} \tag{4.18}$$

where $VV^u = k_{VS} \cdot N_{pool}^{V_3A}(\mathbf{r},t) \cdot N_{pool}^u(\mathbf{r},t)$ is the vibrational energy transfer process rate between V_3A and a thermal pool u (for such bimolecular collisions, $k_i = v\,\sigma_i$), $Wall = k_w(\mathbf{r}) \cdot N_{pool}^{V_3A}(\mathbf{r},t)$ is the wall collision rate from section 4.4, $SPT^i = k_{SPT} \cdot N_i^{V_3A}(\mathbf{r},t)$ is the SPT process rate from a non-thermal state i in V_3A, $VS^i = k_{VS} \cdot N_i^{V_3A}(\mathbf{r},t)/2$ is the V-swap process rate from a non-thermal state i (the other half goes to V_3E thermal pool), and $Diff = D \cdot \nabla_{\mathbf{r}}^2 N_{pool}^{V_3A}(\mathbf{r},t)$ is the spatial diffusion rate. To simplify the redistribution of vibrationally thermalized molecules following a wall collision, a temporary pool $N^{Temp}(\mathbf{r},t)$ was created to accumulate these molecules and instantly redistribute them according to $RD = f_{V_3A} \cdot N^{Temp}(\mathbf{r},t) = f_{V_3A} \cdot \sum_{i \in All} k_w(\mathbf{r}) \cdot N_{pool}^i(\mathbf{r},t)$, where $f_i = g_i \cdot \exp\left(-\frac{E_i}{k_B T}\right) / \sum_{j \in All} g_j \cdot \exp\left(-\frac{E_j}{k_B T}\right)$, and E_j is the energy of j^{th} vibrational level. Thus, following wall collisions molecules are redistributed among the vibrational levels according to a Boltzmann distribution at T = 300K, effectively removing the pump-induced vibrational excitation and returning most molecules to V_0.

The thermal pools of each vibrational level are connected through non-resonant (e.g. $V_3 \rightarrow V_6$) and near-resonant V-split (e.g. $V_3 + V_3 \rightarrow V_0 + 2V_3$) vibrational energy transfer processes. In the model, the source for excess molecules in the thermal pools of V_0 and V_3 is non-thermal molecules transferred through the SPT and V-swap processes. For vibrational levels other than V_0 or V_3, the rate equations of the constituent thermal pools have the same form as Eq. (4.18), except the SPT and the VS terms.

4.6.2 Lasing action

Initially, thermal pools are occupied according to a Boltzmann distribution at 300K, and non-thermal states are initialized to zero. Upon pumping, molecules are excited from L in V_0A to U in V_3A, creating non-zero non-thermal populations (negative in V_0A, positive in V_3A). The non-thermal molecules move into adjacent non-thermal states through dipole-dipole collisions and into the two thermal pools of that vibrational level through SPT and V-swap processes. They may also transfer into the

thermal pools of other vibrational levels through non-resonant and near-resonant collisions, and eventually returned to a T = 300K thermal Boltzmann distribution through collision with the cavity wall.

When the OPFIR laser reaches steady state, all these processes and all spatial diffusion to and from adjacent layers are equilibrated. Since the dominant vibrational relaxation mechanism occurs through wall collisions, diffusion of vibrationally equilibrated molecules away from the wall following wall collisions creates a spatial population gradient: the population density of the thermal pools in V_0 is highest near the wall and decreases away from it, while the population density of the thermal pools in higher-lying vibrational levels is lowest near the cavity wall and increases away from it. Since the pump rate is proportional to $\Delta N_{pump}(\boldsymbol{r}, t)$ [Eq. (4.5)], it is highest near the cavity wall, and so the pump-generated rotational population inversion is also strongest there. The spatial variation of the steady-state (t_∞) effective population inversion $< \Delta N_{inv}(t_\infty) >$ and effective gain $< \gamma >$ are defined as in Ref. [49]:

$$< \Delta N_{inv}(t_\infty) >= \frac{\int_{V_{ACT}} d\boldsymbol{r} |E_0(\boldsymbol{r})|^2 \Delta N_{inv}(\boldsymbol{r}, t_\infty)}{\int_{V_{ACT}} d\boldsymbol{r} |E_0(\boldsymbol{r})|^2}, \tag{4.19}$$

$$< \gamma >=< \Delta N_{inv}(t_\infty) > \frac{\lambda_{THz}^2}{4\pi^2 n^2 \tau_{spont} \Delta\nu_{THz}}. \tag{4.20}$$

$E_0(\boldsymbol{r})$ is the normalized THz E-field intensity at radial position **r**, and the refractive index $n \approx 1$ for the gas. The width of the rotational transition $\Delta\nu_{THz}$ is the pressure-broadened linewidth - except at the lowest pressures (< 100 mTorr) when Doppler broadening dominates - that causes gain to decrease with increasing pressure for a hypothetically fixed inversion. Of course, the magnitude of the inversion $\Delta N_{inv}(\boldsymbol{r}, t_\infty)$ varies significantly with pressure and pump power. V_{ACT} is the volume of active region of the entire cavity, λ_{THz} is the wavelength of the THz lasing output, and τ_{spont} is the spontaneous emission lifetime, which is roughly chosen to be 100 sec for the direct inversion in $^{13}CH_3F$ [66].

There are two cavity loss mechanisms considered in this paper: ohmic loss α_{ohmic} due to E-field penetration into the copper cavity wall, and reflection loss from the

cavity reflectors. Therefore, total loss can be expressed as: $\alpha_{total} = 2\alpha_{ohmic} - \ln(\Gamma_{front}\Gamma_{back})/L_{cell}$, where Γ_{front}, Γ_{back} are the reflectivities of the front and back cavity reflectors [49]. Assuming the copper is 100 % reflective with $\alpha_{ohmic} = 0.0014$ cm^{-1} [67], $\alpha_{total} = 0.0055$ cm^{-1} for an $r = 0.5$ mm diameter coupling hole in a $R = 2.5$ mm cavity whose $\Gamma_{front} = 1 - (\pi r^2/\pi R^2) = 0.96$. Note that there is no loss from un-pumped molecule absorption, as discussed in Section 4.3. The cavity mode that is expected to start lasing first is determined by the total loss α_{total} and the effective gain $< \gamma >$, the latter of which is proportional to the spatial overlap of mode profile and the rotational inversion [Eq. (4.19)]. TE_{01} mode experiences minimum ohmic loss because it is strongly localized in the center of the cavity. TE_{21} mode, on the other hand, has a strong field near the wall, resulting in a greater overlap with the inversion. Although this produces a greater ohmic loss, the loss is offset by the much greater effective gain, which ultimately yields a higher net effective gain (given by $< \gamma >$ - α_{total}). Therefore, TE_{21} is the likely laser mode and is assumed in this paper.

Lasing action occurs as long as the pump-induced difference in non-thermal population is large enough to overcome the corresponding thermal pool contribution and the cavity losses. The cutoff pressure occurs when the high pressure effective gain $< \gamma >$ equals the total loss α_{total}, so the net effective gain is zero. At low pressure, inversion grows with pressure as there are more molecules in L, while rapid wall collisions keep the thermal pool population in V_3 relatively low (hence increasing ΔN_{pump}). As pressure increases, the pump rate eventually stops increasing fast enough to overcome the increased thermal population trapped by a decreasing wall collision rate, and it is near this pressure that the strongest lasing action occurs. Beyond this pressure, inversion starts to decrease with increasing pressure, and eventually a cutoff pressure is reached where the thermal pool quenches the non-thermal population difference to stop lasing action. Therefore, the magnitude of inversion as well as lasing output power shows bell-shape curve with pressure as shown in Fig. 4-6(b). Fig. 4-7 plots the model-predicted effective gain $< \gamma >$ as a function of pressure for the six-level multi-layer model. It shows the total loss and effective gains from both the direct and refilling inversions at three different pump powers: 3.3, 6.6, and 10 W. It is interesting

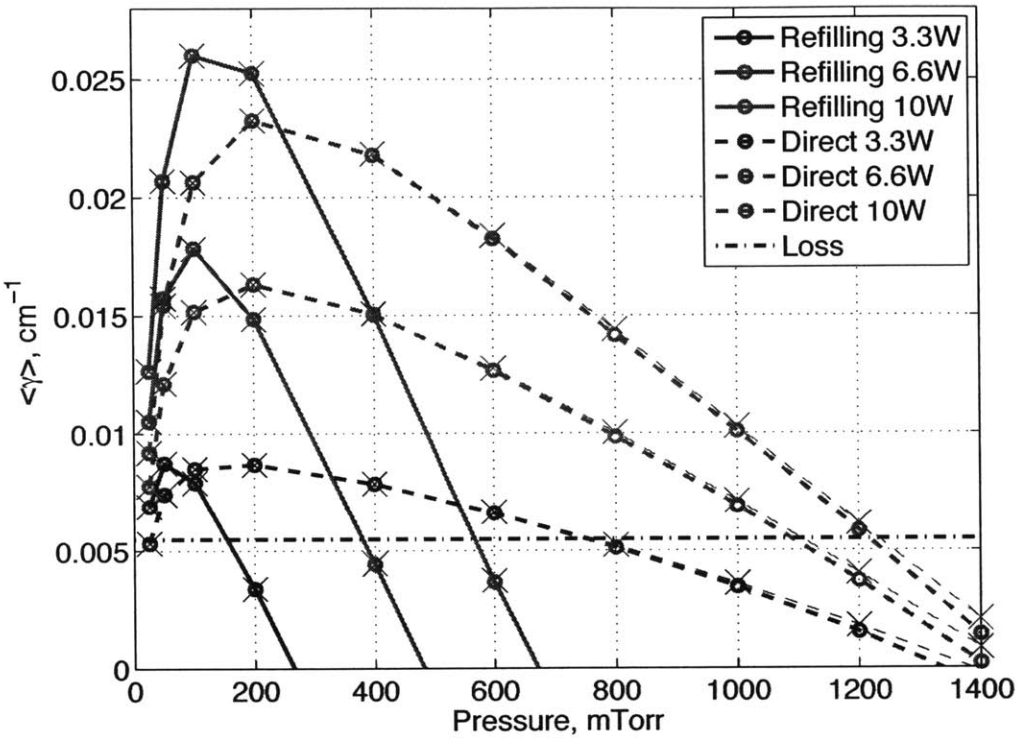

Figure 4-7: Predicted gain $< \gamma >$ for pump powers of 3.3, 6.6, and 10 W obtained from the T_v-model using multi-layer system ('o') and single-layer system ('x'), overlaid by total loss $\alpha_{total} = 0.0055$ cm^{-1}. The effective gain is the amount of gain above this line, and a power-independent cutoff pressure near 1.5 Torr is predicted for the direct inversion.

to note that almost the same effective gains were predicted in the single-layer model too. Lasing occurs when the gain exceeds the loss, and at the lowest pressures the refilling inversion produces more laser power than the direct inversion. However, the thermal pool in V_0 is much larger than in V_3, so the refilling inversion quenches at a lower pressure than the direct inversion. The low-pressure behavior (< 700 mTorr) of the model agrees well with the experimental measurements in Fig. 4-6(b).

Notice that the effective gain and the cutoff pressures for the refilling inversion in Fig. 4-7 increase with increasing pump power: the pump indirectly depletes the quenching V_0A thermal pool when it attempts to refill the non-thermal states being drained by the pump. Conversely, the effective gain for the direct inversion show a

pump power-independent characteristic at high pressures. It is clear from the slope of the lines that effective gain at pressures above 1.7 Torr cannot be achieved for any pump power. Note that the model-predicted cutoff pressures for the direct inversion are significantly higher than the 0.44 Torr predicted from Ref. [50] where only V_0 and V_3 are considered. Clearly the addition of four more vibrational levels in the six-level model has raised the cutoff pressure by providing additional pathways to deplete the V_3 thermal pools, but pump power-independent behavior of effective gain for the direct inversion does not agree with the experimental measurement in Fig. 4-6(b).

Thus, the six-level model of Fig. 4-1 significantly improved the agreement with the experimental data compared to models considering only the lowest two or three vibrational levels. However, the predicted pump-independent cutoff pressure is incorrect because the number of accessible vibrational levels is artificially capped and still not enough. Indeed, it appears that any model containing a limited number of vibrational levels cannot reproduce the pump power-dependent cutoff pressures observed. Clearly more vibrational levels are involved, and they must be added to the model to accommodate all the excited molecules in the high-pressure regime. The number of vibrational levels increases rapidly at higher energy through a growing variety of fundamentals (e.g. V_1, V_2, V_4, V_5), overtones (e.g. $3V_3$, $3V_6$) and combinations (e.g. $2V_3+V_6$, $2V_6+V_3$). Note that these vibrational levels are even higher in energy, yet they clearly contribute to the laser performance.

4.7 High-pressure regime

The inability of any model with a limited number of vibrational levels to reproduce the pump power-dependent cutoff pressure for the direct inversion indicates that the number of molecules excited to higher-lying vibrational levels and the number of vibrational levels involved increases with pump power and especially pressure, as the vibrational bottleneck fills V_3 and V-split type processes become more active. Although more vibrational levels must be added to the model, following the modeling procedure in Section 4.6 would dramatically increase the computation time, and more

importantly, the rate constants connecting all these vibrational levels are unknown.

Instead, we propose to model the contribution of all accessible vibrational levels with one expandable thermal pool which embodies them all, containing separate subpools for the A and E symmetry types. This expandable pool, labeled V_Σ, contains all 120 vibrational levels higher than V_3 up to 6959 cm^{-1}, taking into account the specific energies and degeneracies of each. By including so many vibrational levels, V_Σ eliminates the artificial trapping of population in V_0 and V_3 by simulating the increasingly favorable vibrational redistribution mechanisms that become effective as V_3 fills. Consequently, the reduced thermal pool populations in V_0 and V_3 reduce the inversion quenching and increase the gain, especially in the high-pressure regime.

A schematic diagram of this new model is illustrated in Fig. 4-8(a). There are only six thermal pools: A and E symmetry type pools for each of V_0 (ground), V_3, and V_Σ. The 120 lowest vibrational levels, all below 6959 cm^{-1}, are included in V_Σ. The fractional population in V_Σ is obtained using the Boltzmann vibrational partition function

$$Q_v(T_v) = \sum_j g_j \cdot \exp\left(-\frac{E_j}{k_B T_v}\right). \tag{4.21}$$

To calculate the un-pumped equilibrium population of V_Σ for initial vibrational temperature at T_v = 300K, consider first the fractional population in V_0 and V_3, which is $f^0_{V_0} = 1/Q^0_v$ and $f^0_{V_3} = \exp(-E_{V_3}/k_B T_v)/Q^0_v$, where Q^0_v is defined as $Q_v(T_v)$ at T_v = 300K. From this, it is easy to see

$$f^0_{V_\Sigma} = \frac{1}{Q^0_v} \sum_{i \neq V_0, V_3} g_i \cdot \exp\left(-\frac{E_i}{k_B T_v}\right) = 1 - f^0_{V_0} - f^0_{V_3}. \tag{4.22}$$

For CH_3F at T_v = 300K, $f^0_{V_0}$ = 0.984 and $f^0_{V_3} = 6.43\times10^{-3}$, so $f^0_{V_\Sigma} = 9.56\times10^{-3}$. Because each vibrational level is represented by two symmetry-preserving thermal subpools, each receives half its vibrational level's respective fraction. We will shortly see that these 120 vibrational levels appear to be enough to accommodate excited molecules in the pressure range of our interest, but one can easily add more vibrational levels if required.

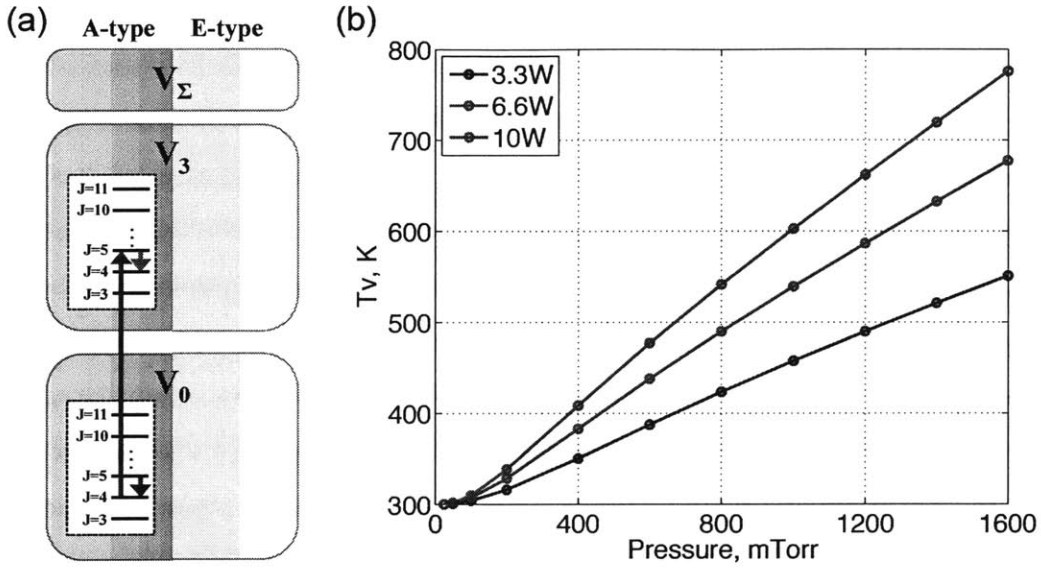

Figure 4-8: (a) T_v-model has total six thermal pools. V_Σ is an expandable thermal pool which combines 120 high-lying vibrational levels. (b) T_v as a function of pressure and power is plotted. T_v represents the distribution of population among the vibrational levels. As pressure and power increases, T_v increases, meaning that more molecules populate V_Σ.

To consider the rate constants connecting V_3 and V_Σ, many more vibrational processes than those listed in Table 4.2 are needed. An alternative and simpler way to represent the net rate between V_3 and V_Σ may be found by applying two fundamental principles that operate when the laser reaches steady state [50]: 1) The number density of molecules being pumped (upward) is equal to number density of molecules returning to V_0 through wall collisions (downward), and 2) the population distribution among the vibrational levels constituting V_Σ may be represented by a single vibrational temperature T_v. The net rate between V_3 and V_Σ is thus chosen to establish that T_v, which grows from $T_v = 300$K when the pump is turned on, eventually to reach a steady-state value that we must ascertain. As a consequence, the model attempts to estimate the final steady-state distribution produced by the pump $ab - initio$ rather than allowing this population to evolve dynamically with time from $T_v = 300$K. The following parts describe an iterative process of finding this steady-state vibrational temperature from these two principles at a given pressure and pump power.

The net rate between V_3 and V_Σ effectively encompasses all vibrational state-changing processes between them. At steady state, every level must have equal incoming and outgoing population densities ($dN/dt = 0$). Likewise, for V_0 the outgoing population density pumped by the IR laser from Eq. (4.3) must be equal to the incoming population density produced from the wall collisions from V_3 and V_Σ. This equilibrium condition may be expressed as:

$$R_{pump} = k_w \left[(N_{V_3} - N^0_{V_3}) + (N_{V_\Sigma} - N^0_{V_\Sigma}) \right], \tag{4.23}$$

where N_{V_3} and N_{V_Σ} are the final steady-state population densities in V_3 and V_Σ, and $N^0_{V_3}$ and $N^0_{V_\Sigma}$ are the initial (before pumping) population densities. Of course, this condition is satisfied when the pump is turned off (when $R_{pump} = 0$, $N_{V_3} = N^0_{V_3}$ and $N_{V_\Sigma} = N^0_{V_\Sigma}$). Since

$$\begin{aligned} N_{V_3} + N_{V_\Sigma} &= N_0(f_{V_3} + f_{V_\Sigma}) = N_0(1 - f_{V_0}) \\ &= N_0 \left(1 - \frac{1}{Q_v} \right) \end{aligned} \tag{4.24}$$

, and similarly $N^0_{V_3} + N^0_{V_\Sigma} = N_0(1 - 1/Q^0_v)$, Eq. (4.23) becomes:

$$R_{pump} = k_w N_0 \left(\frac{1}{Q^0_v} - \frac{1}{Q_v} \right). \tag{4.25}$$

When solved for Q_v,

$$Q_v = \frac{k_w N_0 Q^0_v}{k_w N_0 - R_{pump} \cdot Q^0_v} = \frac{Q^0_v}{1 - \frac{R_{pump} \cdot Q^0_v}{k_w N_0}}. \tag{4.26}$$

At this point Q_v is unknown because R_{pump} in steady state is less than the initial R_{pump} for reasons discussed in Section 4.3. However, it may be assumed that the distribution of population in V_Σ may be characterized by $Q_v(T_v)$ as in Eq. (4.21), where T_v is the final but also unknown steady-state vibrational temperature. Assuming steady state conditions in which the pump moves molecules directly into V_3 and indirectly into

V_Σ and using this unknown Q_v, the net rate constant from V_3 to V_Σ for maintaining steady state must be

$$R_{V_3 \to V_\Sigma} = R_{pump} \cdot \frac{f_{V_\Sigma}}{f_{V_3} + f_{V_\Sigma}} = \frac{R_{pump} \cdot f_{V_\Sigma} \cdot Q_v}{Q_v - 1} , \tag{4.27}$$

because $f_{V_3} + f_{V_\Sigma} = 1 - f_{V_0} = 1 - 1/Q_v = (Q_v - 1)/Q_v$.

The process then is to set an initial guess for T_v as T_v^{init}, from which Q_v^{init} can be found from Eq. (4.21), and the net rate from V_3 to V_Σ can be found from Eq. (4.27). If the initial guess Q_v^{init} is correct, then the condition of Eq. (4.23) is satisfied, and Q_v^{final} calculated from Eq. (4.26) using the steady-state pump rate will be identical to Q_v^{init}. If the initial guess is incorrect, the rate equation model adjusts T_v^{init} until $Q_v^{init} = Q_v^{final}$. Note that $R_{V_3 \to V_\Sigma}$ evolves dynamically as a function of the redistribution of population induced by the pump, whose rate also depends on the redistribution of population through Eq. (4.3). This explains why an iterative approach is necessary.

In this simplified single-layer T_v-model, all other attributes, such as the wall collision rate, population inversion, effective gain, and losses, are inherited from the six-level model described in Section 4.6. The new expandable V_Σ pools and the net rate from V_3 to V_Σ are the main differences between the six-level and the T_v-models. The physical significance of these changes is that 120 vibrational levels (or more as needed) are implicitly involved by introducing an expandable thermal pool V_Σ, which thereby makes the vibrational bottleneck dependent upon the pump power and produces a much higher, pump power-dependent cutoff pressure. One additional benefit is that fewer rate constants are required in the model because all of the vibrational state-changing collisional processes in Table 4.2 and many others are captured in the net rate from V_3 to V_Σ of Eq. (4.27).

As Eq. (4.26) indicates, T_v is also a function of pressure, as plotted in Fig. 4-8(b) for three different pump powers of 3.3, 6.6, and 10 W. The most important insight comes from recognizing that T_v increases with increasing pump power. This means that more molecules reach higher vibrational levels with higher pump powers, so the

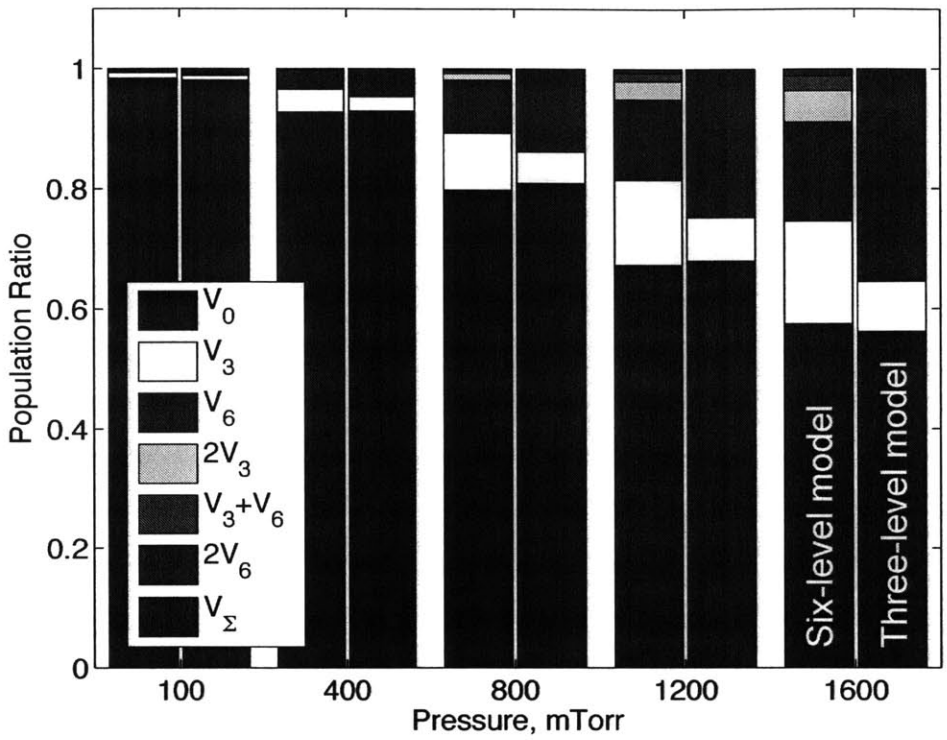

Figure 4-9: Population fraction of each thermal pool in the six-level model (left bars) and in the T_v-model (right bars) at five different pressures and 10W pump power. The difference between the two models in the high-pressure regime shows the important role of V_Σ in the T_v-model. Notice how V_3 is always less populated in the T_v-model.

population density in V_Σ grows. In fact, it grows at a faster rate than the population density in V_3 grows, and this explains why quenching of the inversion and the cutoff pressure depend on the pump power at high pressures. The flaw in previous models now becomes apparent. Because of the fixed number of vibrational levels, previous models generate unphysically high values of the population density in V_3, quenching both the pump rate and the rotational inversion at a lower cutoff pressure. This also explains why the predicted cutoff pressure in those models is less sensitive to pump power: the more V_3 is overfilled through the vibrational bottleneck, the more the pump rate is reduced, reaching a saturation population that is relatively independent of pump power.

To ascertain whether the six-level model truly suffers from artificial trapping of

molecules in the existing vibrational levels and whether the T_v-model alleviates this, consider Fig. 4-9 which shows the fractional population of each vibrational level at steady state for five different pressures and $P_{pump} = 10$ W. For each pressure, the left bar represents the six-level model, and the right bar represents the T_v-model. Since the vibrational bottleneck traps more molecules in excited vibrational levels at high pressure, the portion of V_0 decreases while other thermal pools increase with pressure.

As can be clearly seen from Fig. 4-9, the fractional population differs significantly as pressure increases. For example, the fraction of $V_0/V_3/V_\Sigma$ at 1600 mTorr is 0.56/0.08/0.36, while the fraction of $V_0/V_3/V_6$-$2V_6$ is 0.57/0.17/0.26. Note that V_3 has more than twice the population in the six-level model than in the T_v-model, while the higher excited vibrational levels have only 2/3 the population. This is because molecules that should be distributed in vibrational levels higher than $2V_6$ are artificially trapped among the six vibrational levels in the six-level model. Thus, the six-level model artificially increases the fractional population of V_0 and V_3, which explains the pump power-independent behavior of the direct inversion at high-pressures in Fig. 4-7. Since the higher fraction of molecules in V_0 and V_3 makes it harder for the pump to create population inversions, the six-level model underestimates the high-pressure performance. Not surprisingly, the six-level model predicts a quenched inversion, while the three level model predicts gain in agreement with experimental measurements.

The effective gain and the total loss calculated from the T_v-model is plotted in Fig. 4-10. The model prediction shows the behavior of both types of inversion (direct and refilling), and it agrees well with the experimental results in Fig. 4-6(b). The refilling inversion dominates in the low-pressure regime, and the direct inversion is dominant in mid- and high-pressure regime. Since V_0 has much more thermal population than V_3, the refilling inversion is quenched earlier than the direct inversion. Increasing pump power generally increases net effective gain at a given pressure. Bell-shape curves were obtained from both the model and the experiment, both of which indicate that higher pressure operation is possible with higher pump

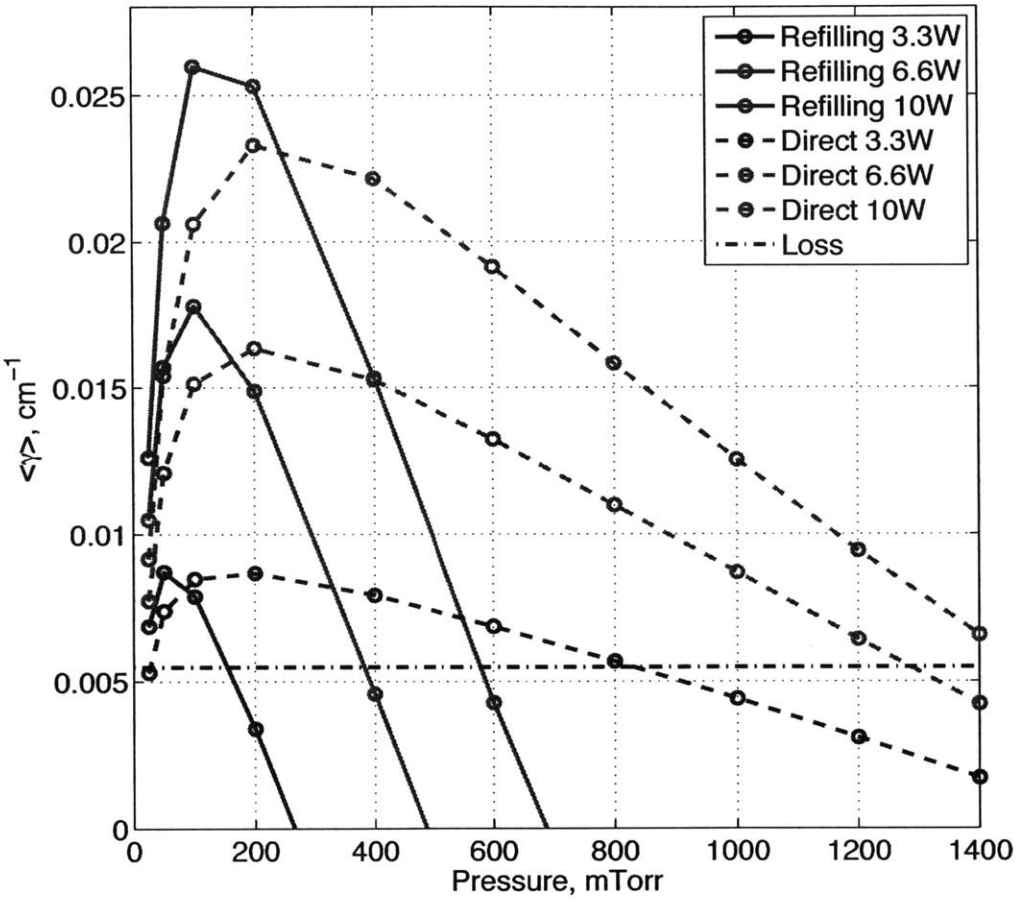

Figure 4-10: Predicted gain as a function of pressure and pump power from the T_v-model, overlaid by the total cavity loss. Both refilling and direct inversions are predicted, and their behavior matches very well with the experimental measurement in Fig. 4-6(b). The refilling inversion dominates in the low-pressure regime, but only the direct inversion operates in the high-pressure regime. The model prediction of the cutoff pressure (occurring when gain equals loss) quantitatively agrees with the experiment.

powers. Cutoff pressures predicted by the model occur when the gain curves cross the loss line, and the values match very well with the experiment. This quantitative and qualitative agreement between the model prediction and the experiment confirm that the T_v-model involving an increasing number of vibrational levels can accurately simulate pump power-dependent lasing action of OPFIR systems.

It is worth noting the differences between Fig. 4-7, the predictions from the six-level model, and Fig. 4-10, the predictions from the T_v-model. They show basic agreement in low-pressure regime, but deviate in high-pressure regime. V_Σ in the T_v-model contains 120 vibrational levels compared to the six-level model; therefore, it provides extra channels for molecules in V_0 and V_3 to be redistributed. As shown in Fig. 4-9, this effect becomes more significant in high-pressure regime. Since molecules are not artificially trapped in V_0 and V_3 in the T_v-model, vibrational bottleneck can depend on pump power, and the inversions can survive to higher pressures. The T_v-model involves significantly fewer rate equations and avoids the need to know hundreds of collisional cross sections. If these were required, the six-level model involving 30 rate equations would become the 122-level model requiring 262 rate equations and 7,442 unknown collisional cross sections. Instead, the T_v-model only requires 24 rate equations for which all the collisional cross sections are known.

4.8 Concluding remarks

We have reported a comprehensive theoretical analysis of THz lasing action in optically-pumped rotationally excited $^{13}CH_3F$ molecular gases confined in a copper cavity. We have shown how an expanded version of the six-level model developed in Ref. [49] cannot accurately predict the high-pressure behavior of the system, and we introduced a new T_v-model that effectively reproduces the experimentally observed behavior at all pressures and pump powers. The T_v-model includes an expandable thermal pool V_Σ to mimic the environment of having numerous high-lying vibrational levels, and we derived the rate constant connecting that pool to V_3 using equilibrium conditions. This model is advantageous in that it does not require detailed knowledge of state-

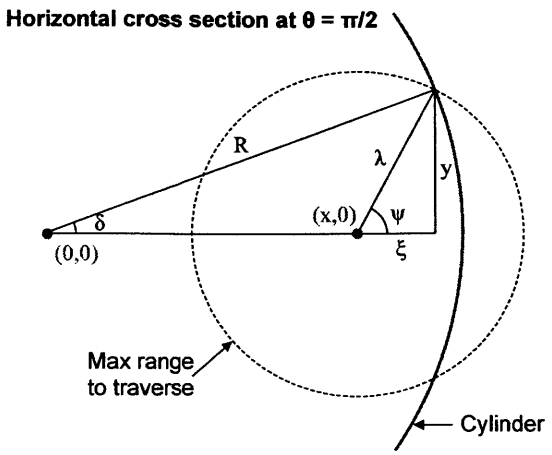

Figure 4-11: This is a plot of the horizontal cavity cross section (blue line) and the maximum range a molecule can traverse in one λ (dashed line) starting at $(x, 0)$ for $x \in [R - \lambda, R]$.

to-state rates among the high-lying vibrational levels, since they are all captured in one net rate, $R_{V_3 \to V_\Sigma}$. The model prediction of the lasing output was verified experimentally, and we observed qualitatively and quantitatively correct behavior of both direct and refilling inversions. This model could contribute to the development of compact sources of far-infrared and THz radiation and may be used to design novel, spatially non-uniform cavity designs to improve the performance of high-power THz lasing sources.

4.9 Appendix: Wall Collision Rate

4.9.1 Maximum radial angle, $\psi(\theta)$

I assume a spherical coordinate centered at $(x, 0)$ where the molecule is located. In the spherical coordinate, polar angle θ measures an angle from a fixed zenith direction that passes through $(x, 0)$.

At $\theta = \pi/2$ (as shown on Fig. 4-11),

$$\sin\psi = \frac{y}{\lambda}, \quad \sin\delta = \frac{y}{R} \rightarrow \quad \sin\delta = \left(\frac{\lambda}{R}\right)\sin\psi \tag{4.28}$$

$$\cos\psi = \frac{\xi}{\lambda}, \quad \cos\delta = \frac{x+\xi}{R} \rightarrow \quad \cos\delta = \frac{x+\lambda\cos\psi}{R} \tag{4.29}$$

$$\sin^2\delta + \cos^2\delta = 1 \tag{4.30}$$

$$\left(\frac{\lambda}{R}\right)^2 \sin^2\psi + \left(\frac{x+\lambda\cos\psi}{R}\right)^2 = 1 \tag{4.31}$$

$$\lambda^2 + x^2 + 2x\lambda\cos\psi - R^2 = 0 \tag{4.32}$$

$$\therefore \cos\psi = \frac{R^2 - \lambda^2 - x^2}{2x\lambda}. \tag{4.33}$$

Horizontal cavity cross section at $\theta \neq \pi/2$ will be the same as Fig. 4-11, but only the radius of maximum range to traverse will change to $\lambda\sin\theta$. Therefore, the maximum radial angle ψ is a function of θ.

$$\cos\psi(\theta) = \frac{R^2 - (\lambda\sin\theta)^2 - x^2}{2x(\lambda\sin\theta)} \tag{4.34}$$

$$\therefore \psi(\theta) = \cos^{-1}\left[\frac{R^2 - (\lambda\sin\theta)^2 - x^2}{2x(\lambda\sin\theta)}\right] \tag{4.35}$$

4.9.2 Minimum polar angle, θ_0

From Fig. 4-12,

$$\sin\theta_0 = \frac{R-x}{\lambda} \tag{4.36}$$

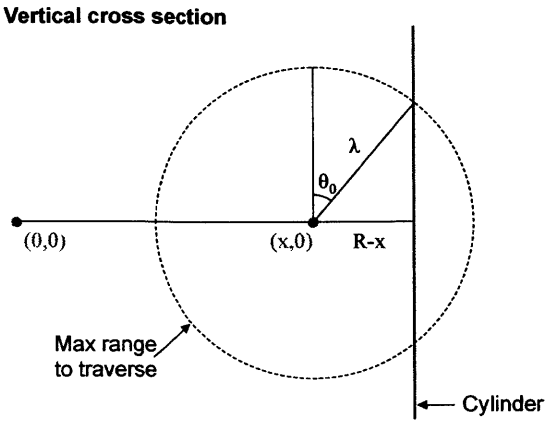

Figure 4-12: This is a plot of the vertical cavity cross section (blue line) and the maximum range a molecule can traverse. It shows the minimum polar angle θ_0.

$$\therefore \theta_0 = \sin^{-1}\left[\frac{R-x}{\lambda}\right] \tag{4.37}$$

Therefore, integrating polar angle range is $[\theta_0, \pi/2]$.

4.9.3 Collisional fraction, $f_w(x)$

Since all molecules can travel λ, the ratio of molecules hitting the wall is equal to the fraction of the area that intercepts the cavity wall. Here, this fraction is calculated as a function of cavity radius R and mean free path λ for a molecule located at (x, 0).

The upper half of intercepting area $F(x)$ is expressed as below. $A(x)$ is the intercepting area of a band with polar angle θ. As shown in Fig. 4-13, its length is equal to $\lambda \sin\theta \times 2\psi(\theta)$ and its width is equal to $\lambda d\theta$. $F(x)$ is, therefore, the integration of $A(x)$ within $\theta \in [\theta_0, \pi/2]$. $\psi(\theta)$ and θ_0 are derived in section 4.9.1 and 4.9.2, respectively.

$$\begin{aligned} F(x) &= \int_{\theta_0}^{\pi/2} A(x,\theta)\,\mathrm{d}\theta = \int_{\theta_0}^{\pi/2} \lambda\sin\theta \cdot 2\psi(\theta) \cdot \lambda \mathrm{d}\theta \\ &= \int_{\theta_0}^{\pi/2} 2\lambda^2 \sin\theta \cos^{-1}\left(\frac{R^2 - (\lambda\sin\theta)^2 - x^2}{2x(\lambda\sin\theta)}\right) \mathrm{d}\theta \end{aligned} \tag{4.38}$$

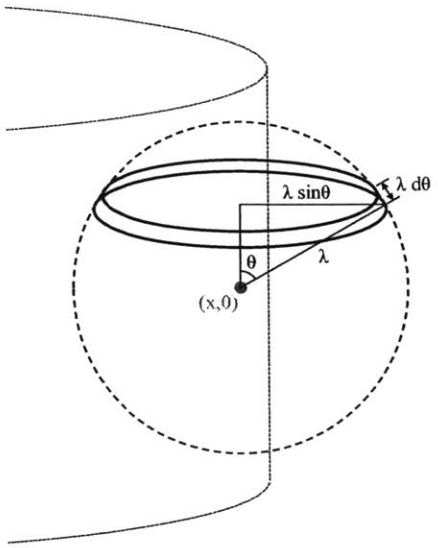

Figure 4-13: This is a plot of the cylindrical cavity (blue line) and the maximum range a molecule can traverse (black dashed line). To calculate the fraction of the area intercepting the cavity wall, the spherical shell is divided in z-direction.

$$\therefore f_w(x) = \frac{2 \cdot F(x)}{4\pi\lambda^2} \tag{4.39}$$

4.9.4 Average distance to the wall, $\bar{l}(x)$

At a given x, θ, ϕ, the distance to the wall $l(x, \theta, \psi')$ can be divided into two parts: $l(x, \theta, \psi') = \sqrt{l_\perp^2 + l_\parallel^2}$. $l_\perp$ represents the vertical part, and $l_\parallel$ represents the horizontal one. From the left hand side of Fig. 4-14, $l_\perp$ can be easily shown as:

$$l_\perp = \frac{R - x}{\tan\theta}\,. \tag{4.40}$$

Note the analogy to Fig. 4-11 and the right hand side of Fig. 4-14. Thus, we can say,

$$\cos\psi' = \frac{R^2 - l_\parallel^2 - x^2}{2\,x\,l_\parallel} \tag{4.41}$$

$$l_\parallel = -x\cos\psi' + \sqrt{x^2\cos^2\psi' - x^2 + R^2}\,. \tag{4.42}$$

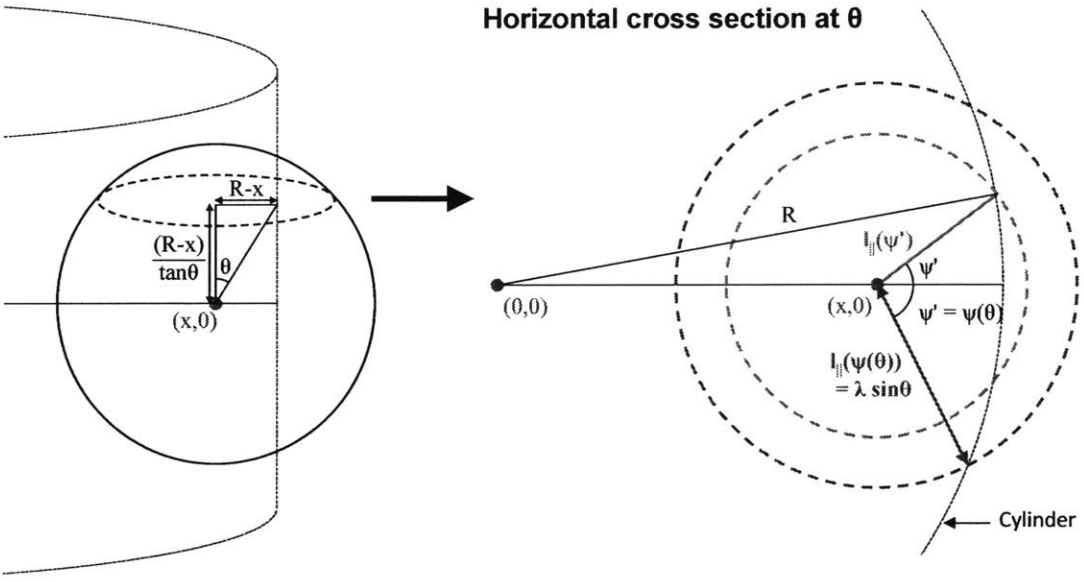

Figure 4-14: On the left hand side is a plot of the cavity (blue dotted line) and the maximum range a molecule can traverse. It shows that the distance to the wall varies with the polar angle θ. On the right hand side is a plot of the horizontal cross section at θ. The distance to the wall also varies with the azimuthal angle ψ'. Green dotted line represents the maximum horizontal range a molecule with a polar angle θ can traverse, which is equal to $\lambda \sin\theta$.

Hence, the average distance $\bar{l}(x)$ from x to the wall can be expressed as the integration of $l(x,\theta,\psi')$ over the range of angles divided by the solid angle. (Only the first octant space is integrated for simplicity.)

$$\begin{aligned}\bar{l}(x) &= \frac{\int_{\theta_0}^{\pi/2}\int_0^{\psi(\theta)} l(x,\theta,\psi')\cdot\sin\theta\,\mathrm{d}\psi'\,\mathrm{d}\theta}{\int_{\theta_0}^{\pi/2}\int_0^{\psi(\theta)}\sin\theta\,\mathrm{d}\psi'\,\mathrm{d}\theta} \\ &= \frac{\int_{\theta_0}^{\pi/2}\int_0^{\psi(\theta)}\sqrt{\left(\frac{R-x}{\tan\theta}\right)^2+\left(-x\cos\psi'+\sqrt{x^2\cos^2\psi'-x^2+R^2}\right)^2}\cdot\sin\theta\,\mathrm{d}\psi'\,\mathrm{d}\theta}{\int_{\theta_0}^{\pi/2}\int_0^{\psi(\theta)}\sin\theta\,\mathrm{d}\psi'\,\mathrm{d}\theta}\end{aligned} \tag{4.43}$$

Note that $l_{\|}$ has to satisfy two boundary conditions. As shown on the right hand side of Fig. 4-14, when $\psi'=0$, $l_{\|}$ has to be equal to $R-x$, and when $\psi'=\psi(\theta)$, $l_{\|}$ has to be equal to $\lambda\sin\theta$.

Proof. When $\psi'=0$,

$$\begin{aligned}l_{\|} &= -x\cos\psi'+\sqrt{x^2\cos^2\psi'-x^2+R^2} \\ &= -x+\sqrt{x^2-x^2+R^2}=R-x\end{aligned} \tag{4.44}$$

□

Proof. When $\psi'=\psi(\theta)=\cos^{-1}\left[\frac{R^2-(\lambda\sin\theta)^2-x^2}{2x(\lambda\sin\theta)}\right]$,

$$
\begin{aligned}
l_{\parallel} &= -x\cos\psi' + \sqrt{x^2\cos^2\psi' - x^2 + R^2} \\
&= -\frac{R^2 - (\lambda\sin\theta)^2 - x^2}{2(\lambda\sin\theta)} + \sqrt{\left(\frac{R^2 - (\lambda\sin\theta)^2 - x^2}{2(\lambda\sin\theta)}\right)^2 - x^2 + R^2} \\
&= -\frac{1}{2\lambda\sin\theta}\left[R^2 - (\lambda\sin\theta)^2 - x^2 - \sqrt{\left(R^2 - (\lambda\sin\theta)^2 - x^2\right)^2 + (R^2 - x^2)\cdot(2\lambda\sin\theta)^2}\right] \\
&= -\frac{1}{2\lambda\sin\theta}\left[R^2 - (\lambda\sin\theta)^2 - x^2 - \sqrt{\left(R^2 - x^2 + (\lambda\sin\theta)^2\right)^2}\right] \\
&= -\frac{1}{2\lambda\sin\theta}\left[R^2 - (\lambda\sin\theta)^2 - x^2 - \left(R^2 - x^2 + (\lambda\sin\theta)^2\right)\right] \\
&= -\frac{1}{2\lambda\sin\theta}\left[-2(\lambda\sin\theta)^2\right] \\
&= \lambda\sin\theta
\end{aligned}
\tag{4.45}
$$

□

4.9.5 Average time to reach the wall, $\tau(x)$

From section 4.9.4, we derived the average distance to the wall from a position x, $\bar{l}(x)$. The time to reach the wall τ, however, depends on the velocity. Assuming molecules' speed is Maxwell-Boltzmann distributed, the average time to reach the wall is a weighted average of $\tau(x, v)$.

$$
\tau(x, v) = \frac{\bar{l}(x)}{v} \tag{4.46}
$$

$$
\begin{aligned}
\tau(x) &= \int_0^\infty \tau(x, v)\cdot f_{MB}(v)\,\mathrm{d}v \\
&= \int_0^\infty \tau(x, v)\cdot 4\pi\left[\frac{m}{2\pi k_B T}\right]^{3/2} v^2 \exp\left[-\frac{mv^2}{2k_B T}\right]\,\mathrm{d}v
\end{aligned}
\tag{4.47}
$$

4.9.6 Wall collision rate, $k_w(x)$

Wall collision rate k_w is simply,

$$k_w(x) = \frac{f_w(x)}{\tau(x)}\,. \tag{4.48}$$

$f_w(x)$ and $\tau(x)$ are derived in section 4.9.3 and 4.9.5, respectively.

Chapter 5

Conclusion & Outlook

In this thesis, we presented the fabrication and numerical simulation of laser sources.

We first experimentally verified the existence of unique high-Q modes that are singly degenerate at Γ. We fabricated 2D square-lattice photonic crystals with cylindrical holes on silicon nitride wafers, and measured their reflectivity in a range of angles. By stacking the reflectivity graphs with respect to the angle, we obtained the photonic band diagram. By fitting the resonance peaks to the theoretical reflectivity formula, we were able to extract Q^{total} values and track how each mode's Q changes with the angle. In this way, we experimentally verify the existence of the unique high-Q bound states embedded in the continuum of extended modes. Moreover, we concluded that the observed Q^{total} is limited by $Q_{non-rad}$ which comes from any imperfections in fabrication.

Therefore, the fabrication optimization steps are presented next. Through the optimization, we obtained three times higher Q values. This involves innovation in IL tool, materials, RIE parameters, post-development treatment, and optical measurement tool. We also explored e-beam lithography, but its low throughput makes IL an ideal tool for large-area, high-Q, defect-free 1D&2D photonic crystal fabrication. I believe that the fabrication process can be further improved and enhance attainable Q^{total} in the future. For example, by expanding the IL laser beams to a wider angle or by shaping the beam profile to a more uniform distribution, spatial power distribution will become uniform, and spatial variation of the pattern will

be decreased. Post-process thin dielectric film coating using atomic layer deposition might also improve Q by mitigating surface roughness.

We next presented the numerical simulation of high-pressure lasing action in optically-pumped rotationally excited molecular gases. Previous theoretical models under-predicted the lasing output in high-pressure regime because of the vibrational bottleneck. The vibrational bottleneck comes from lack of channels to dissipate the pumped molecules. Adding a few numbers of vibrational levels to provide additional channels for them was not enough to avoid the vibrational bottleneck. Our completely new three-level model includes an expandable vibrational model, which effectively represents 120 vibrational levels. The rate constant related to this new level was derived from the equilibrium conditions. Since there are enough channels for the excited molecules, the vibrational bottleneck was not observed in the three-level model, and its model prediction agrees with the experiment not only qualitatively but also quantitatively. The model can be universally used for any OPFIR laser gas systems, and we believe that the model could contribute to the development of room-temperature atmospheric-pressure compact sources of far-infrared and THz radiation. Current three-level model assumes single-layer, which can model only spatially uniform system. In the future, we believe that novel spatially non-uniform cavity designs, which can be simulated by three-level multi-layer model, should be explored to improve the performance of high-power THz lasing sources.

Bibliography

[1] Jeongwon Lee, Bo Zhen, Song-Liang Chua, Wenjun Qiu, John D. Joannopoulos, Marin Soljačić, and Ofer Shapira. Observation and differentiation of unique high-q optical resonances near zero wave vector in macroscopic photonic crystal slabs. *Physical Review Letters*, 109(6):067401, Aug 2012.

[2] Jeongwon Lee, Bo Zhen, Song-Liang Chua, Ofer Shapira, and Marin Soljačić. Fabricating centimeter-scale high quality factor two-dimensional periodic photonic crystal slabs. *Optics Express*, 22(3):3724–3731, Feb 2014.

[3] Chia Wei Hsu, Bo Zhen, Jeongwon Lee, Song-Liang Chua, Steven G. Johnson, John D. Joannopoulos, and Marin Soljačić. Observation of trapped light within the radiation continuum. *Nature*, 499(7457):188–191, 07/11 2013.

[4] Bo Zhen, Song-Liang Chua, Jeongwon Lee, Alejandro W. Rodriguez, Xiangdong Liang, Steven G. Johnson, John D. Joannopoulos, Marin Soljačić, and Ofer Shapira. Enabling enhanced emission and low-threshold lasing of organic molecules using special fano resonances of macroscopic photonic crystals. *Proceedings of the National Academy of Sciences*, 2013.

[5] Song-Liang Chua, Bo Zhen, Jeongwon Lee, Jorge Bravo-Abad, Ofer Shapira, and Marin Soljačić. Modeling of threshold and dynamics behavior of organic nanostructured lasers. *Journal of Materials Chemistry C*, 2(8):1463–1473, 2014.

[6] J. D. Joannopoulos, S. G. Johnson, R. D. Meade, and J. N. Winn. *Photonic Crystals: Molding the Flow of Light.* Princeton Univ. Press, Princeton, NJ, 2008.

[7] O. Painter, J. Vuckovic, and A. Scherer. Defect modes of a two-dimensional photonic crystal in an optically thin dielectric slab. *Journal of the Optical Society of America B*, 16(2):275–285, Feb 1999.

[8] H. Cao Y. Yamamoto, F. Tassone. *Semiconductor Cavity Quantum Electrodynamics*, volume 169. Springer, 2000.

[9] Reginald K. Lee, Yong Xu, and Amnon Yariv. Modified spontaneous emission from a two-dimensional photonic bandgap crystal slab. *Journal of the Optical Society of America B*, 17(8):1438–1442, Aug 2000.

[10] Alexei A. Erchak, Daniel J. Ripin, Shanhui Fan, Peter Rakich, John D. Joannopoulos, Erich P. Ippen, Gale S. Petrich, and Leslie A. Kolodziejski. Enhanced coupling to vertical radiation using a two-dimensional photonic crystal in a semiconductor light-emitting diode. *Applied Physics Letters*, 78(5):563–565, 2001.

[11] Susumu Noda, Mitsuru Yokoyama, Masahiro Imada, Alongkarn Chutinan, and Masamitsu Mochizuki. Polarization mode control of two-dimensional photonic crystal laser by unit cell structure design. *Science*, 293(5532):1123–1125, 2001.

[12] Masayuki Fujita, Shigeki Takahashi, Yoshinori Tanaka, Takashi Asano, and Susumu Noda. Simultaneous inhibition and redistribution of spontaneous light emission in photonic crystals. *Science*, 308(5726):1296–1298, 2005.

[13] A. Rosenberg, Michael Carter, J. Casey, Mijin Kim, Ronald Holm, Richard Henry, Charles Eddy, V. Shamamian, K. Bussmann, Shouyuan Shi, and Dennis Prather. Guided resonances in asymmetrical gan photonic crystal slabs observed in the visible spectrum. *Optics Express*, 13(17):6564–6571, Aug 2005.

[14] Susumu Noda, Masayuki Fujita, and Takashi Asano. Spontaneous-emission control by photonic crystals and nanocavities. *Nature Photonics*, 1(8):449–458, print 2007.

[15] Dirk Englund, Andrei Faraon, Ilya Fushman, Nick Stoltz, Pierre Petroff, and Jelena Vuckovic. Controlling cavity reflectivity with a single quantum dot. *Nature*, 450(7171):857–861, 2007.

[16] M. Ghebrebrhan, P. Bermel, Y. X. Yeng, I. Celanovic, M. Soljacic, and J. D. Joannopoulos. Tailoring thermal emission via q matching of photonic crystal resonances. *Physical Review A*, 83(3):033810, Mar 2011.

[17] Song-Liang Chua, Yidong Chong, A. Douglas Stone, Marin Soljačić, and Jorge Bravo-Abad. Low-threshold lasing action in photonic crystal slabs enabled by fano resonances. *Optics Express*, 19:1539–1562, 2011.

[18] P. Paddon and Jeff F. Young. Two-dimensional vector-coupled-mode theory for textured planar waveguides. *Physical Review B*, 61(3):2090–2101, Jan 2000.

[19] T. Ochiai and K. Sakoda. Dispersion relation and optical transmittance of a hexagonal photonic crystal slab. *Physical Review B*, 63(12):125107, Mar 2001.

[20] Shanhui Fan and J. D. Joannopoulos. Analysis of guided resonances in photonic crystal slabs. *Physical Review B*, 65(23):235112, 2002.

[21] V. Pacradouni, W. J. Mandeville, A. R. Cowan, P. Paddon, Jeff F. Young, and S. R. Johnson. Photonic band structure of dielectric membranes periodically textured in two dimensions. *Physical Review B*, 62(7):4204–4207, Aug 2000.

[22] Ehsan Shah Hosseini, Siva Yegnanarayanan, Mohammad Soltani, and Ali Adibi. Ultra-high quality factor microdisk resonators for chip-scale visible integrated photonics. In *Frontiers in Optics*, page FMG4. Optical Society of America, 2008.

[23] Ardavan F. Oskooi, David Roundy, Mihai Ibanescu, Peter Bermel, J. D. Joannopoulos, and Steven G. Johnson. Meep: A flexible free-software package for electromagnetic simulations by the fdtd method. *Computer Physics Communications*, 181(3):687–702, 3 2010.

[24] Jean-Pierre Berenger. A perfectly matched layer for the absorption of electromagnetic waves. *Journal of Computational Physics*, 114(2):185–200, Oct 1994.

[25] Kazuaki Sakoda. *Optical Properties of Photonic Crystals.* Springer, 2001.

[26] J. M. Pottage, E. Silvestre, and P. St. J. Russell. Vertical-cavity surface-emitting resonances in photonic crystal films. *Journal of the Optical Society of America A*, 18(2):442–447, Feb 2001.

[27] David L. C. Chan, Ivan Celanovic, J. D. Joannopoulos, and Marin Soljacic. Emulating one-dimensional resonant q-matching behavior in a two-dimensional system via fano resonances. *Physical Review A*, 74(6):064901, 12/22 2006.

[28] Kerry J. Vahala. Optical microcavities. *Nature*, 424:839–846, 2003.

[29] TrevorM Benson, SvetlanaV Boriskina, Phillip Sewell, Ana Vukovic, StephenC Greedy, and AlexanderI Nosich. *Micro-optical resonators for microlasers and integrated optoelectronics*, volume 216 of *Frontiers in Planar Lightwave Circuit Technology*, pages 39–70. Springer Netherlands, 2006.

[30] D. K. Armani, T. J. Kippenberg, S. M. Spillane, and K. J. Vahala. Ultra-high-q toroid microcavity on a chip. *Nature*, 421:925–928, 2003.

[31] Jiangang Zhu, Sahin Kaya Ozdemir, Yun-Feng Xiao, Lin Li, Lina He, Da-Ren Chen, and Lan Yang. On-chip single nanoparticle detection and sizing by mode splitting in an ultrahigh-q microresonator. *Nature Photonics*, 4:46–49, 2010.

[32] O. Painter, R. K. Lee, A. Scherer, A. Yariv, J. D. O'Brien, P. D. Dapkus, and I. Kim. Two-dimensional photonic band-gap defect mode laser. *Science*, 284:1819–1821, 1999.

[33] Masahiro Nomura, Satoshi Iwamoto, Katsuyuki Watanabe, Naoto Kumagai, Yoshiaki Nakata, Satomi Ishida, and Yasuhiko Arakawa. Room temperature continuous-wave lasing in photonic crystal nanocavity. *Optics Express*, 14:6308–6315, 2006.

[34] Bong-Shik Song, Susumu Noda, Takashi Asano, and Yoshihiro Akahane. Ultra-high-q photonic double-heterostructure nanocavity. *Nature Materials*, 4:207–210, 2005.

[35] Yasushi Takahashi, Yoshinori Tanaka, Hiroyuki Hagino, Tomoyuki Sugiya, Yoshiya Sato, Takashi Asano, and Susumu Noda. Design and demonstration of high-q photonic heterostructure nanocavities suitable for integration. *Optics Express*, 17:18093–18102, 2009.

[36] Andrea M. Armani, Rajan P. Kulkarni, Scott E. Fraser, Richard C. Flagan, and Kerry J. Vahala. Label-free, single-molecule detection with optical microcavities. *Science*, 317:783–787, 2007.

[37] Tymon Barwicz, Miloš Popović, Peter Rakich, Michael Watts, Hermann Haus, Erich Ippen, and Henry Smith. Microring-resonator-based add-drop filters in sin: fabrication and analysis. *Optics Express*, 12:1437–1442, 2004.

[38] Tymon Barwicz, Miloš Popović, Michael R. Watts, Peter T. Rakich, Erich P. Ippen, and Henry I. Smith. Fabrication of add-drop filters based on frequency-matched microring resonators. *Journal of Lightwave Technology*, 24:2207–2218, 2006.

[39] Corey P. Fucetola, Hasan Korre, and Karl K. Berggren. Low-cost interference lithography. *Journal of Vacuum Science and Technology B*, 27(6):2958–2961, November 2009 2009.

[40] Q. Xie, M. H. Hong, H. L. Tan, G. X. Chen, L. P. Shi, and T. C. Chong. Fabrication of nanostructures with laser interference lithography. *Journal of Alloys and Compounds*, 449:261–264, 2008.

[41] Henry I. Smith. Low cost nanolithography with nanoaccuracy. *Physica E*, 11:104–109, 2001.

[42] Alex Buxbaum and Melvin W. Montgomery. U.S. Patent No. 6,582,861 B2, 24 June 2003.

[43] Michael Gehl, Ricky Gibson, Joshua Hendrickson, Andrew Homyk, Antti Säynätjoki, Tapani Alasaarela, Lasse Karvonen, Ari Tervonen, Seppo Honkanen, Sander Zandbergen, Benjamin C. Richards, J. D. Olitzky, Axel Scherer, Galina Khitrova, Hyatt M. Gibbs, Ju-Young Kim, and Yong-Hee Lee. Effect of atomic layer deposition on the quality factor of silicon nanobeam cavities. *Journal of the Optical Society of America B*, 29:A55–A59, 2012.

[44] J. O. Henningsen and H. Jensen. The optically pumped far-infrared laser: Rate equations and diagnostic experiments. *IEEE Journal of Quantum Electronics*, 11(6):248–252, Jun 1975.

[45] D. Dangoisse, P. Glorieux, and J. Wascat. Diffusion and vibrational bottleneck in optically pumped submillimetre lasers. *International Journal of Infrared and Millimeter Waves*, 2(2):215–229, 1981.

[46] Mary S. Tobin. A review of optically pumped nmmw lasers. *Proceedings of the IEEE*, 73(1):61–85, Jan 1985.

[47] T. Y. Chang and T. J. Bridges. Laser action at 452, 496, and 541 μm in optically pumped ch_3f. *Optics Communications*, 1(9):423, 1970.

[48] T. Plant, Leon A. Newman, E. Danielewicz, T. DeTemple, and P. Coleman. High power optically pumped far infrared lasers. *IEEE Transactions on Microwave Theory and Techniques*, 22(12):988–990, Dec 1974.

[49] Song-Liang Chua, Christine A. Caccamise, Dane J. Phillips, John D. Joannopoulos, Marin Soljačić, Henry O. Everitt, and Jorge Bravo-Abad. Spatio-temporal theory of lasing action in optically-pumped rotationally excited molecular gases. *Optics Express*, 19(8):7513–7529, Apr 2011.

[50] Henry O. Everitt, David D. Skatrud, and Frank C. De Lucia. Dynamics and tunability of a small optically pumped cw far-infrared laser. *Applied Physics Letters*, 49(16):995–997, 1986.

[51] R. McCormick, Henry O. Everitt, Frank C. De Lucia, and David D. Skatrud. Collisional energy transfer in optically pumped far-infrared lasers. *IEEE Journal of Quantum Electronics*, 23(12):2069–2077, Dec 1987.

[52] Henry O. Everitt and Frank C. De Lucia. A time-resolved study of rotational energy transfer into a and e symmetry species of $^{13}ch_3f$. *The Journal of chemical physics*, 90(7):3520–3527, 1989.

[53] Henry O. Everitt and Frank C. De Lucia. Rotational energy transfer in ch_3f: The $\delta z = n$, $\delta k = 0$ processes. *The Journal of chemical physics*, 92(11):6480–6491, 1990.

[54] Richard L. Crownover, Henry O. Everitt, Frank C. De Lucia, and David D. Skatrud. Frequency stability and reproducibility of optically pumped far-infrared lasers. *Applied Physics Letters*, 57(27):2882–2884, 1990.

[55] Henry O. Everitt and Frank C. De Lucia. The temperature dependence of fast vibrational energy transfer processes in methyl fluoride. *Molecular Physics*, 79(5):1087–1101, 1993.

[56] Henry O. Everitt and Frank C. De Lucia. Rotational energy transfer in small polyatomic molecules. *Advances in Atomic, Molecular, and Optical Physics*, 35:331–400, 1995.

[57] William H. Matteson and Frank C. De Lucia. Millimeter wave spectroscopic studies of collision-induced energy transfer processes in the $^{13}ch_3f$ laser. *IEEE Journal of Quantum Electronics*, 19(8):1284–1293, Aug 1983.

[58] William H. Matteson and Frank C. De Lucia. Millimeter-wave studies of the $^{13}ch_3f$ laser: the effects of buffer gases and the spectroscopy of the laser states. *Journal of the Optical Society of America B*, 2(2):336–342, 1985.

[59] R. McCormick, Frank C. De Lucia, and David D. Skatrud. A time-resolved study of rotational and vibrational excitation and relaxation in the $^{13}ch_3f$ optically pumped far-infrared laser. *IEEE Journal of Quantum Electronics*, 23(12):2060–2068, Dec 1987.

[60] Henry O. Everitt. *Collisional energy tranfer in methyl halides.* PhD thesis, Duke University, 1990.

[61] *See Appendix for more thorough derivation of the wall collision rate.*

[62] J. O. Hirschfelder, C. F. Curtiss, and R. B. Bird. *Molecular theory of gases and liquids.* Wiley, 1954.

[63] R. J. Temkin and D. R. Cohn. Rate equations for an optically-pumped, far infrared laser. *Optics Communications*, 16(2):213, 1976.

[64] Takeshi Oka. Unknown yet. *Advances in Atomic and Molecular Physics*, 9:127–206, 1980.

[65] Rekha Sapre Sheorey and George Flynn. Collision dynamics of intermode energy flow in laser pumped polyatomic molecules: Ch_3f. *The Journal of chemical physics*, 72(2):1175–1186, 1980.

[66] Irwin Shamah and George Flynn. Vibrational relaxation induced population inversions in laser pumped polyatomic molecules. *Chemical Physics*, 55(1):103–115, 1981.

[67] A. J. Baden Fuller. *Microwaves : an introduction to microwave theory and techniques.* Oxford, 1990.